Astrocytic LRRK2 Controls Synaptic Connectivity through ERM Phosphorylation.

Shiyi Wang[1], Dhanesh Sivadasan Bindu[1], Christabel Xin Tan[1], Kristina Sakers[1,9], Tetsuya Takano[2,3], Maria Pia Rodriguez[1], Kylie Dimond[1,9], Scott H. Soderling[1,4,5], Albert R. La Spada[6,7,8], and Cagla Eroglu[1, 4, 5, 9]

[1]The Department of Cell Biology, Duke University Medical Center, Durham, NC, USA

[2]The Department of Neurophysiology, Keio University School of Medicine, Japan

[3]Japan Science and Technology Agency, PRESTO, Japan

[4]The Department of Neurobiology, Duke University Medical Center, Durham, NC, USA

[5]Aligning Science Across Parkinson's (ASAP) Collaborative Research Network, Chevy Chase, MD

[6]The Department of Neurology, Duke University Medical Center, Durham, NC, USA

[7]Departments of Pathology & Laboratory Medicine, Neurology, Biological Chemistry, University of California, Irvine, CA, USA

[8]UCI Center for Neurotherapeutics, University of California, Irvine, CA, USA

[9]Howard Hughes Medical Institute, Duke University Medical Center, Durham, NC, USA

Corresponding authors: Shiyi Wang: shiyi.wang@duke.edu;

Albert R. La Spada: alaspada@uci.edu;

Cagla Eroglu: cagla.eroglu@duke.edu

Abstract

Astrocytes tightly control neuronal connectivity and function in the brain through direct contact with synapses[1-5]. These glial cells become reactive during disease pathogenesis[6-8] including Parkinson's disease (PD)[9-14]. However, it remains unknown if astrocyte dysfunction is an initiating factor of PD pathogenesis and whether astrocytes can be targeted to stop or reverse the synaptic dysfunction seen in PD. Using *in vitro* and *in vivo* methods, we found that the PD-linked gene Lrrk2 controls astrocyte morphology via regulating the phosphorylation of ERM proteins (Ezrin, Radixin, and Moesin), a structural component of the perisynaptic astrocyte processes. ERM phosphorylation is robustly elevated both in mice and humans carrying the LRRK2 G2019S Parkinsonism mutation. Importantly, the reduction of the ERM phosphorylation, specifically in the LRRK2 G2019S in adult astrocytes, is sufficient to restore excitatory synapse number and function deficits in the LRRK2 G2019S knock-in mouse cortex. These results show a role for Lrrk2 in controlling astrocyte morphogenesis and synaptogenic function and reveal that early astrocyte dysfunction in PD could be causal to disruptions in cortical excitatory synaptic connectivity. The astrocytic dysfunction can be corrected by dampening ERM phosphorylation, pinpointing astrocytes as critical cellular targets for PD therapeutics.

Main Text

Astrocytes instruct the formation and function of synaptic circuits[3,12,15]. Most synapses in the central nervous system are in direct contact with perisynaptic astrocyte processes[16-19]. This structural association is essential for the regulation of synaptic function; therefore, the perisynaptic astrocyte process and the pre- and postsynaptic neuronal compartments were coined the term “the tripartite synapse”[18,20]. At the tripartite synapse, astrocytes clear excess neurotransmitters, maintain ion homeostasis, and secrete factors regulating synapse development and function[21-25]. To accomplish these crucial roles at the synapse, astrocytes gain a highly elaborate morphology and form a network coupled through gap junctions to continuously tile the entire brain parenchyma[2,19,26]. Previous studies found that astrocyte morphogenesis, tiling, and neuronal synaptogenesis are interdependent processes controlled by bidirectional signaling via secreted factors and cell adhesion molecules[27-32].

Astrocytes become reactive in numerous neurological disorders, including Parkinson’s Disease (PD)[33,34]. PD is a progressive neurodegenerative motor disorder affecting over 8 million people worldwide[35-37]. PD is commonly diagnosed at the onset of motor symptoms, including tremors, bradykinesia, and rigidity. By the time these motor symptoms are apparent, the PD patients have already lost many of their dopaminergic neurons in their substantia nigra pars compacta (SNPc)[38,39]. However, decades before the onset of motor dysfunction, individuals with PD often display non-motor symptoms, such as cognitive, mood, and sleep disorders[40-43]. These clinical observations suggest that during the early phases of PD, synaptic circuit dysfunction exists across multiple brain regions, including the cerebral cortex[44,45]. Recent studies suggested that astrocytes

61 contribute to neurodegeneration in PD by producing neurotoxic factors, increasing
62 glutamate-mediated excitotoxicity, disrupting K^+ buffering and Ca^{2+} homeostasis[10,46,47].
63 However, it remains unknown if astrocyte dysfunction is an initiating factor or a reaction
64 to neuronal pathology in PD.

65 **Astrocytic LRRK2 controls astrocyte morphology through ERM phosphorylation.**

66 Even though most PD cases are idiopathic, ~15% are caused by mutations in
67 Parkinsonism genes[48]. The PD-linked genes identified to date point to dysfunction in
68 fundamental cellular processes such as lysosome and mitochondria function, vesicular
69 trafficking, and secretion[49-51]. However, how the dysfunction of these genes results in
70 impaired synaptic circuits and dopaminergic neuron death is unknown. Moreover, many
71 cell types in the brain and body express these PD-linked genes[52-54]. Thus, the cellular
72 origins of PD may not be restricted to neurons.

73 Mutations in the leucine-rich repeat kinase 2 (*LRRK2*) gene cause familial PD[55,56].
74 In particular, the LRRK2 G2019S is the most common mutation that causes familial
75 PD[43,49,57]. It is largely accepted that LRRK2 G2019S is a gain-of-function mutation that
76 increases LRRK2's kinase activity[58-63]. PD patients with the LRRK2 G2019S mutation
77 exhibit symptoms and disease progression that resembles idiopathic PD, such as late-
78 onset disease, responsiveness to L-DOPA treatment, and the presence of Lewy body
79 and Tau-tangle pathology[64,65]. PD patients with the LRRK2 G2019S mutation also have
80 non-motor symptoms, such as depression, hallucinations, and sleep and cognitive
81 disorders[43,57,66]. Several rodent models with LRRK2 G2019S mutation have been
82 generated; however, these models do not show motor dysfunction or dopaminergic

83 neuron loss[67-69]. However, non-motor symptoms such as cognitive dysfunction is
84 common in PD, indicating impairments in numerous brain regions, including the cerebellar
85 cortex[70,71]. Previous human and rodent studies showed that LRRK2 is highly expressed
86 in the cortex and LRRK2 G2019S alters cortical and cortico-striatal circuits and causes
87 cognitive problems such as impaired goal-directed actions, reflecting critical non-motor
88 symptoms of PD[72-81].

89 Because astrocytes play essential roles in cortical circuit formation and function[5,82],
90 and cortical connectivity is altered in PD, we tested whether mouse and rat cortical
91 astrocytes express Lrrk2. Using a knockout (KO)-verified LRRK2 antibody[83,84], we
92 visualized the expression of Lrrk2 protein in cortical mouse astrocytes by immunostaining
93 coronal brain sections from wild-type (WT) or LRRK2 G2019S knock-in ($^{ki/ki}$) mice[76,85].
94 These mice also contained the Aldh1l1-eGFP transgene[28], labeling all astrocytes with
95 GFP. Lrrk2 staining was evident in both WT and LRRK2 G2019S mouse astrocytes,
96 localizing throughout astrocytic processes (Extended Data Fig. 1a-b). Similarly, cortical
97 astrocytes from WT or LRRK2 G2019S BAC transgenic rats also express Lrrk2 *in vitro,*
98 which we verified by immunoblotting (Extended Data Fig. 1c-d; Extended Data Fig. 1e-f).

99 To investigate the function of LRRK2 in astrocyte morphogenesis, we first utilized
100 a primary rat cortical astrocyte and neuron co-culture system to examine how the loss of
101 Lrrk2 affects astrocyte morphology. To do so, we knocked down Lrrk2 with a short hairpin
102 RNA (shRNA) that targets both the rat and mouse *Lrrk2* (Extended Data Fig. 1g-h). In this
103 neuron-astrocyte co-culture assay, we isolated WT (unmanipulated) cortical neurons and
104 astrocytes from neonatal rats and cultured them separately for 9 days *in vitro* (DIV).
105 Astrocytes were then transfected with GFP-tagged shRNA against *Lrrk2* (sh*Lrrk2*) or a

106 scrambled control shRNA (shControl). Two days post-transfection, astrocytes were
107 plated onto DIV11 WT neurons (Fig. 1a). As previously shown[28,86], astrocytes transfected
108 with shControl acquired a complex morphology in response to 48 hours of neuronal
109 contact (Fig. 1b). On the contrary, Lrrk2 knockdown stunted astrocyte morphological
110 complexity (Fig. 1b). To avoid possible off-target effects from shRNA, we also isolated
111 cortical astrocytes from LRRK2 KO rats[87-90]. We examined their morphological complexity
112 in response to contact with WT neurons. Like sh*Lrrk2* astrocytes, LRRK2 KO astrocytes
113 had significantly diminished arborization compared to WT rat astrocytes, indicating that
114 Lrrk2 is required for neuron-induced astrocyte morphogenesis *in vitro* (Fig. 1b).

115 To study how LRRK2 G2019S affects astrocyte morphological complexity, we
116 isolated cortical astrocytes from WT or LRRK2 G2019S BAC-transgenic rats[87-89] and
117 examined their morphological complexity in response to contact with WT neurons *in vitro*.
118 We found that LRRK2 G2019S rat astrocytes showed a reduction in astrocyte complexity
119 compared to WT astrocytes (Fig. 1c-d). These results suggest that both loss and gain of
120 LRRK2 kinase function impair astrocyte morphogenesis *in vitro*.

121 To determine if neuronal LRRK2 G2019S mutation could impact astrocyte
122 morphogenesis in a cell non-autonomous manner, we cocultured WT or LRRK2 G2019S
123 astrocytes with LRRK2 G2019S neurons. When cultured on top of LRRK2 G2019S
124 neurons, the WT astrocytes also displayed reduced arborization, indicating that LRRK2
125 G2019S mutation bi-directionally impairs astrocyte-neuron signaling required for
126 astrocyte morphogenesis (Fig. 1c-d). These results show that LRRK2 G2019S impairs
127 astrocyte morphology in both a cell-autonomous and non-cell autonomous manner,

128 illustrating important roles for astrocytic and neuronal Lrrk2 function in establishing proper
129 astrocyte-neuron contacts.

130 Lrrk2 is a large multidomain protein containing ROC (Ras of complex), COR (C-
131 terminal of ROC), catalytic kinase, and 4 protein-protein interactions domains (armadillo,
132 ankyrin, leucine-rich repeats, WD40 domains)[64,91,92]. The PD-linked mutation, LRRK2
133 G2019S, is in the kinase domain and is known to increase LRRK2 kinase activity *in vitro*
134 and *in vivo*[58-60,62]. Previous studies identified numerous intracellular proteins (Rab8A,
135 Rab10, endophilin A1, auxillin, ribosomal protein s15, N-ethylmaleimide sensitive fusion
136 protein, synaptojanin, and P62/SQSTM1) as LRRK2 kinase substrates[62,93-99]. LRRK2
137 plays critical roles in ciliogenesis, lysosome function, immune system, and synaptic
138 vesicle trafficking by phosphorylation of its substrates[100-115].

139 ERM proteins (Ezrin, Radixin, and Moesin) are structural components of
140 perisynaptic astrocyte processes (PAPs)[16,17]. LRRK2 phosphorylates a conserved
141 threonine residue present in all ERM proteins[60,116,117]. When phosphorylated, ERM
142 proteins change conformation and link the F-actin cytoskeleton to the cell membrane[118,119].
143 This switch is thought to play an important role in organizing cell morphology by allowing
144 process outgrowth[119,120]. Among the ERM proteins, ezrin is specifically and highly
145 enriched in astrocytes (Extended Data Fig. 1i-j) and is known to preferentially localize at
146 the perisynaptic astrocyte processes[16]. Genetic ablation or down regulation of ezrin has
147 been shown to reduce astrocyte morphological complexity *in vivo*[121-123]. Given these
148 potential functional links between LRRK2 and ERM proteins, we wondered whether Lrrk2
149 controls astrocyte morphology via ERM phosphorylation (phospho-ERM).

150 To determine if LRRK2 function in astrocytes is required for ERM phosphorylation,
151 we analyzed the levels of phospho-ERM in WT rat astrocytes treated with two different
152 doses of MLi-2, a highly specific LRRK2 kinase inhibitor and compared phospho-ERM
153 levels to the vehicle (DMSO) treated astrocyte cultures using immunoblotting. The well-
154 established LRRK2 phosphorylation substrate Rab10 served as a control for this
155 assay[61,100,103]. As expected, MLi-2 treatment inhibited Rab10 phosphorylation (Fig. 1e).
156 We found that, compared to astrocytes treated with DMSO, both 30 and 100 nM MLi-2
157 treatment decreased phospho-ERM levels in WT rat astrocytes by ~75%, indicating that
158 LRRK2 kinase function is required for ERM phosphorylation in astrocytes (Fig. 1f). Next,
159 we compared the levels of ERM phosphorylation in astrocytes isolated from WT or LRRK2
160 G2019S rats and found an increase (increased by ~100%) in ERM phosphorylation in
161 LRRK2 G2019S astrocytes (Fig. 1g-h). These data reveal an important role for LRRK2 in
162 mediating ERM phosphorylation in astrocytes *in vitro*. These findings also suggest that
163 LRRK2 controls astrocyte morphology by regulating ERM phosphorylation levels.

164 **ERM phosphorylation state underlies Lrrk2-mediated astrocyte morphological**
165 **complexity.**

166 Because both loss of Lrrk2 function (shRNA and LRRK2 KO) and gain of Lrrk2
167 kinase function (LRRK2 G2019S) perturbed astrocyte morphogenesis, we hypothesized
168 that a balance between phosphorylated and unphosphorylated ERM protein levels may
169 be crucial for regulating astrocyte morphological complexity. To test this hypothesis, we
170 manipulated the balance between phosphorylated and unphosphorylated ERM in
171 sh*Lrrk2*-transfected or LRRK2 G2019S astrocytes using two EZRIN mutants with

172 phosphorylation-mimicking or -deficient properties. Switching the amino acid threonine (T)
173 at location 567 with aspartate (D) results in a conformation of EZRIN that mimics a
174 constitutively phosphorylated state[124,125]. On the other hand, mutating the same residue
175 T567 to alanine (A) results in a version of the protein that cannot be phosphorylated:
176 phospho-dead EZRIN[119,120]. Phospho-dead EZRIN binds to the plasma membrane like
177 WT EZRIN but is poorly associated with the actin cytoskeleton[119,120,126,127].

178 We first tested if overexpressing phospho-mimetic EZRIN in sh*Lrrk2*-transfected
179 astrocytes would rescue their morphology. Astrocytes transfected with shControl, and WT
180 EZRIN or phospho-mimetic EZRIN served as controls. In these experiments, only
181 astrocytes were manipulated and plated onto WT rat neurons. WT or phospho-mimetic
182 EZRIN transfection did not change the morphological complexity of shControl astrocytes
183 (Fig. 1i). However, overexpression of phospho-mimetic EZRIN, but not WT EZRIN, fully
184 rescued the complexity of sh*Lrrk2* astrocytes (Fig. 1j).

185 We next tested if increasing unphosphorylated EZRIN would rescue the
186 morphogenesis of LRRK2 G2019S astrocytes. To do so, we isolated cortical astrocytes
187 from WT or LRRK2 G2019S rats, and over-expressed WT or phospho-dead EZRIN, and
188 plated transfected astrocytes on WT cortical neurons. We found that overexpression of
189 WT EZRIN did not change the morphology of WT or LRRK2 G2019S astrocytes. However,
190 overexpression of the phospho-dead EZRIN reduced the morphological complexity of WT
191 astrocytes (Fig. 1k). Conversely, overexpression of the phospho-dead EZRIN fully
192 rescued the morphological complexity of LRRK2 G2019S astrocytes *in vitro* (Fig. 1l).
193 These results show that LRRK2 mediates astrocyte morphological complexity by
194 regulating ERM phosphorylation and strongly suggest that the balance between

195 phosphorylated and unphosphorylated ERM proteins is needed for neuronal contact-
196 induced astrocyte morphogenesis.

197 To determine if LRRK2 G2019S mutation impacts ERM phosphorylation in
198 astrocytes *in vivo*, we examined the levels of phospho-ERM in coronal brain sections from
199 21-day-old (P21) and 12-week-old WT or LRRK2 G2019S$^{ki/ki}$ mice in which astrocytes
200 were labeled via the Aldh1L1-eGFP transgene. When compared to WTs, we observed an
201 increase in phospho-ERM staining in both P21 and 12-week-old LRRK2 G2019S$^{ki/ki}$ mice.
202 This increase was not uniform but rather localized exclusively to some of the astrocytes
203 within the layers L1 and L2/3 of the anterior cingulate cortex (ACC) and the primary motor
204 cortex (MOp) (Fig. 2a-c; Extended Data Fig. 2a-b). In P21 LRRK2 G2019S$^{ki/ki}$ mice, the
205 phospho-ERM integrated densities in the ACC Layer 1 and Layer 2/3 and the MOp Layer
206 1 and Layer 2/3 were increased by ~412% and ~158% compared to the WTs, respectively
207 (Fig. 2d). In 12-week-old (P84) LRRK2 G2019S$^{ki/ki}$ mice, the phospho-ERM integrated
208 densities in the ACC Layer 1 and Layer 2/3 and in the MOp Layer 1 and Layer 2/3 were
209 increased by ~700% and ~398% compared to the WTs, respectively (Extended Data Fig.
210 2c). However, the phospho-ERM integrated density in neighboring brain regions such as
211 the primary somatosensory cortex (SSp) and dorsal medial striatum (DMS) was not
212 different between LRRK2 G2019S$^{ki/ki}$ or WTs (Extended Data Fig. 2h). These findings
213 show that LRRK2 G2019S mutation induces aberrant ERM phosphorylation in astrocytes.
214 Intriguingly, this increase in ERM phosphorylation is not uniform but rather localized to
215 ACC and MOp, which are cortical regions that are impacted in PD patients[128-130].

216 To determine the *in vivo* functions of astrocytic Lrrk2, we examined astrocyte
217 morphological complexity in Layer 1 and Layer 2/3 of ACC and MOp of LRRK2 G2019S$^{ki/ki}$

218 mice. To do so, we used postnatal astrocyte labeling by electroporation (PALE) combined
219 with the PiggyBac transposon system to introduce a membrane-targeted fluorescent label
220 (mCherry-CAAX) into a sparse population of cortical astrocytes in WT and LRRK2
221 G2019S$^{ki/ki}$ mice at P0 (Extended Data Fig. 2k). At P21, following the period of astrocyte
222 growth and extensive elaboration, the territory volumes for LRRK2 G2019S astrocytes
223 were significantly smaller (reduced by ~34%) than WT astrocytes (Fig. 2f). In addition,
224 compared to WT astrocytes, the branching complexity of LRRK2 G2019S astrocytes was
225 reduced (Fig. 2g). The reduction in astrocyte size and complexity in LRRK2 G2019S$^{ki/ki}$
226 astrocytes did not result in an increase in the numbers of astrocytes in these brain regions.
227 (Extended Data Fig. 3a-e). The number of Aldh1L1-EGFP/Sox9 double-positive
228 astrocytes in these brain regions was similar in WT and LRRK2 G2019S$^{ki/ki}$ mice
229 (Extended Data Fig. 3c). However, there were patches within ACC and MOp parenchyma
230 in LRRK2 G2019S$^{ki/ki}$ mice in which the EGFP-positive astrocyte processes had
231 noticeably reduced. These changes in astrocytes were not due to a typical reactive gliosis
232 phenotype because we did not detect any increase in the levels of GFAP, which
233 differentially labels reactive astrocytes in the cortical grey matter (Extended Data Fig. 3f).
234 Taken together, these results reveal that LRRK2 G2019S mutation reduces astrocyte
235 morphological complexity without affecting astrocyte numbers or reactivity *in vivo*.

236 To determine if LRRK2 G2019S-mediated astrocyte morphological deficits are due
237 to the phospho-ERM upregulation in astrocytes, we tested whether phospho-dead EZRIN
238 can rescue the morphological complexity of LRRK2 G2019S astrocytes *in vivo*. To do so,
239 we performed PALE to introduce mCherry-CAAX and phospho-dead EZRIN into
240 astrocytes of WT or LRRK2 G2019S$^{ki/ki}$ mice. Like our *in vitro* results, the overexpression

241 of phospho-dead EZRIN in WT astrocytes is sufficient to decrease the territory volume
242 and morphological complexity (Fig. 2e-g). However, the overexpression of phospho-dead
243 EZRIN restored LRRK2 G2019S astrocyte territory volume and complexity (Fig. 2f-g).
244 These results indicate that balancing phosphorylated and unphosphorylated ERM levels
245 is crucial for regulating astrocyte morphology, and overexpression of phospho-dead
246 EZRIN can rescue morphological deficits of LRRK2 G2019S astrocytes *in vivo*.

247 To further test this hypothesis, we studied if knocking down LRRK2 in WT
248 astrocytes affects astrocyte morphological complexity *in vivo*. We introduced shControl
249 or sh*Lrrk2* into a sparse population of cortical astrocytes in WT mice by using PALE. We
250 found that, like LRRK2 G2019S astrocytes, sh*Lrrk2* astrocytes had significantly smaller
251 territory volumes (reduced by ~36%) and reduced morphological complexity when
252 compared to shControl astrocytes (Fig. 2h-j). To determine whether phospho-mimetic
253 EZRIN can restore astrocyte morphology in LRRK2 knockdown astrocytes *in vivo*, we
254 performed PALE to introduce either sh*Lrrk2* or shControl together with phospho-mimetic
255 EZRIN overexpression vector into astrocytes of the ACC and MOp. We found that over-
256 expression of phospho-mimetic EZRIN in shControl astrocytes did not change astrocyte
257 territory volume (Fig. 2h-i). However, expression of phospho-mimetic EZRIN in sh*Lrrk2*-
258 containing astrocytes restored astrocyte territory volume and morphological complexity
259 up to the WT levels (Fig. 2j). Taken together, these findings revealed that the balance
260 between phosphorylated and unphosphorylated ERM is crucial for LRRK2-mediated
261 astrocyte morphological complexity *in vivo*. Disrupting the balance of ERM
262 phosphorylation status in astrocytes compromises astrocyte morphological complexity,

263 and modulation of this balance can be used to restore astrocyte morphology in the LRRK2
264 G2019S genotype.

265 **ERM phosphorylation is upregulated in the frontal cortices of PD patients carrying**
266 **LRRK2 G2019S mutation.**

267 To determine if phospho-ERM abundance is altered in PD patients carrying LRRK2
268 G2019S mutation, we stained frontal cortices from 3 patients who carry this mutation and
269 compared them to age and sex-matched donors (Supplemental Table 1). We observed
270 that, compared to sex and age-matched human control subjects, the overall levels of
271 phosphorylated ERM were robustly increased by 7-fold in the frontal cortex of PD patients
272 carrying the LRRK2 G2019S mutation (Fig. 2m). The elevated signal of phospho-ERM is
273 often surrounded by GFAP positive astrocytes and astrocyte processes. The astrocytic
274 organization, determined by GFAP staining, appeared to be disrupted in PD patients
275 carrying the LRRK2 G2019S mutation (Fig. 2l). We observed increased GFAP levels in
276 grey matter astrocytes (increased by ~42%) of LRRK2 G2019S mutation carriers,
277 suggesting the presence of reactive gliosis in PD patients carrying LRRK2 G2019S
278 mutation (Fig. 2n). These data indicate that ERM phosphorylation is dysregulated in PD
279 patients carrying the LRRK2 G2019S mutation. Together, our data show that phospho-
280 ERM levels are elevated in the cortices of PD patients with LRRK2 G2019S mutation. The
281 increase in phospho-ERM is concurrent with reactive gliosis and astrocyte morphology
282 changes. Distinct from the P21 and 3-month-old LRRK2 G2019S$^{ki/ki}$ mice where phospho-
283 ERM was restricted to astrocytes, in the human patient brains (~80 years old), we also
284 saw phospho-ERM accumulation outside the GFAP-labelled astrocytes. This observation

285 suggests a role for aberrant ERM phosphorylation in multiple cell types in later stages of
286 PD caused by the LRRK2 G2019S mutation.

287 **LRRK2 G2019S mutation disrupts excitatory and inhibitory synapse numbers and**
288 **function in the cortex.**

289 Astrocyte morphological complexity is a crucial indicator of proper astrocyte-synapse
290 interactions that control synapse numbers[2,27,131-133]. LRRK2 G2019S$^{ki/ki}$ mice revealed no
291 dopaminergic neuron loss or motor dysfunction[68,69]; however, synapse dysfunction at
292 cortico-striatal circuits was observed in adult mice. For example, LRRK2 G2019S alters
293 presynaptic glutamatergic transmission and disrupts glutamate receptor trafficking at
294 striatal postsynaptic terminals[72,76,85,134-136]. However, whether LRRK2 G2019S affects
295 cortical connectivity is unknown. Given the critical role of LRRK2 in synapses and PD-
296 related cortical circuits[137-141], we next investigated the role of LRRK2 G2019S mutation in
297 synaptic connectivity in the ACC and MOp (Fig. 3a). To quantify the density of structural
298 cortical synapses, we used the Vesicular Glutamate Transporter 1 (VGlut1) and the
299 postsynaptic density protein 95 (PSD95) or the Vesicular GABA Transporter (VGAT), and
300 gephyrin (GEPHYRIN), which mark the respective pre- and post-synaptic compartments
301 of intracortical excitatory and inhibitory synapses[142-146] (Fig. 3b). Structural synapses
302 were identified as the apposition and co-localization of pre and postsynaptic markers,
303 which are in two distinct neuronal compartments (i.e., axons and dendrites) and would
304 only appear to co-localize at synapses due to their close proximity[147].

305 Synapse densities were quantified in the Layers 1 and 2/3 of the ACC and MOp of
306 12-week-old LRRK2 G2019S$^{ki/ki}$ and WT mice. There was a significant decrease (~30%)
307 in the VGluT1/PSD95-positive excitatory synapse densities in the ACC of the LRRK2

308 G2019S$^{ki/ki}$ mice compared to WT controls, whereas the VGAT/GEPHYRIN-positive
309 inhibitory synapse numbers in the ACC were not different between genotypes (Fig. 3c-d;
310 Extended Data Fig. 4a-b). On the other hand, we found no changes in the densities of
311 VGluT1/PSD95-positive excitatory synapses in the Layers 1 and 2/3 of the MOp in LRRK2
312 G2019S$^{ki/ki}$ mice compared to WT controls (Extended Data Fig. 4c-d). However,
313 compared to the 12-week-old WT controls, the density of VGAT/ GEPHYRIN-positive
314 inhibitory synapses in Layer 1 and in Layer 2/3 of MOp of LRRK2 G2019S$^{ki/ki}$ mice were
315 increased by ~45% and ~35%, respectively (Fig. 3e-f). These data indicate that LRRK2
316 G2019S mutation differentially impacts the excitatory and inhibitory synapse densities in
317 the ACC and the MOp.

318 We next tested the effects of altered synapse density in the ACC and the MOp of
319 LRRK2 G2019S mice on synaptic function using electrophysiology. To do so, we
320 recorded miniature excitatory postsynaptic currents (mEPSCs) in the ACC and miniature
321 inhibitory postsynaptic currents (mIPSCs) in the MOp layer 2/3 pyramidal neurons from
322 acute brain slices of 12-week-old LRRK2 G2019S$^{ki/ki}$ and WT mice. In agreement with a
323 reduction in excitatory synapse density in the ACC, LRRK2 G2019S$^{ki/ki}$ neurons displayed
324 reduced mEPSC frequency by ~65% and a corresponding right shift in the cumulative
325 distributions of mEPSC inter-event intervals (Fig. 3g-h) when compared to WT neurons.
326 There were no significant changes in the mean mEPSC amplitude or the cumulative
327 probability between genotypes (Fig. 3i). mEPSC frequency changes correlate with
328 changes in synapse numbers or the probability of presynaptic glutamate release[148],
329 whereas the mEPSC amplitude is an indicator of the synaptic strength reflecting the
330 number of AMPARs at the synapse[149]. Therefore, together with our anatomical data,

331 these physiological analyses reveal that LRRK2 G2019S reduced the number of
332 intracortical excitatory connections made onto the Layer 2/3 pyramidal neurons in the
333 ACC without a major change in the synaptic strength.

334 In the MOp motor cortex, on the other hand, we found a robust increase (~73%) in
335 mIPSC frequency when we recorded from the Layer 2/3 pyramidal neurons of the LRRK2
336 G2019S$^{ki/ki}$ mice compared with WT, with no significant change in the amplitude (Fig. 3j-
337 l). The increased mIPSC frequency aligns with our findings that inhibitory synapse
338 numbers are elevated in the MOp of the LRRK2 G2019S mice. This increase could be a
339 result of enhanced inhibitory synaptogenesis or a local increase in the number of
340 inhibitory interneurons in this brain region.

341 Altogether, these electrophysiological and neuroanatomical analyses show that
342 LRRK2 G2019S reduces the density and the function of excitatory synaptic inputs made
343 onto the ACC Layer 2/3 but increases the density and the function of inhibitory synaptic
344 inputs made onto the MOp Layer 2/3. These data are in accordance with our finding that
345 LRRK2 G2019S decreases excitatory synapse numbers in the ACC but increases
346 inhibitory synapse numbers in the MOp. Furthermore, these results suggest that LRRK2
347 kinase function is critical to control proper excitatory and inhibitory synapse development
348 and function in the cortex.

349 **Phospho-dead EZRIN rescues excitatory synapse density in the ACC of adult**
350 **LRRK2 G2019S$^{ki/ki}$ mice.**

351 Because in LRRK2 G2019S$^{ki/ki}$ mice, all cell types, including astrocytes and
352 neurons, express the mutant LRRK2, the cellular origin of the synaptic phenotypes is
353 unclear. Moreover, if these synaptic phenotypes can be rescued by manipulating

354 astrocytes in the adult brain is unknown. Given the robust effects of phospho-dead EZRIN
355 on rescuing LRRK2 G2019S astrocyte morphology, we sought to test whether
356 manipulating the balance of ERM phosphorylation in adult LRRK2 G2019S astrocytes
357 can reverse the synaptic phenotypes we observed in the ACC or MOp of the LRRK2
358 G2019S$^{ki/ki}$ mice.

359 To do so, 9-week-old WT and LRRK2 G2019S$^{ki/ki}$ mice were retro-orbitally injected
360 with AAVs to express Hemagglutinin (HA)-tagged WT EZRIN or phospho-dead EZRIN
361 under the control of the astrocyte-specific GfaABC1D promoter (Extended Data Fig. 5a).
362 The injected mouse brains were harvested at 12 weeks (3 weeks after injection) for
363 synapse quantification, and electrophysiology (Extended Data Fig. 5a). The widespread
364 viral expression of EZRIN proteins in ACC astrocytes was verified by staining with anti-
365 HA tag antibody (Extended Data Fig. 5b). Overexpression of WT EZRIN in WT mouse
366 brains did not cause a noticeable increase in phospho-ERM levels in the cortex. However,
367 WT EZRIN overexpression was accompanied by intense phospho-ERM elevation in the
368 LRRK2 G2019S$^{(ki/ki)}$ cortices. Whereas overexpression of the phospho-dead EZRIN
369 eliminated the phospho-ERM elevation in the LRRK2 G2019S$^{ki/ki}$ cortex (Extended Data
370 Fig. 5b). This observation indicates that overexpression of phospho-dead EZRIN
371 suppresses the elevation of ERM phosphorylation in the LRRK2 G2019S$^{ki/ki}$ cortices.

372 Overexpression of WT EZRIN was not sufficient to rescue the excitatory synapse
373 density decline in layer 1 and layer 2/3 ACC of the LRRK2 G2019S$^{ki/ki}$ mice. However,
374 overexpression of phospho-dead EZRIN reduced excitatory synapse density in the WT
375 background by around 30% (Fig. 4a-b). Strikingly, astrocytic overexpression of phospho-
376 dead EZRIN in the LRRK2 G2019S$^{ki/ki}$ fully rescued the excitatory synapse numbers up

377 to WT levels in ACC layer 1 and layer 2/3 (Fig. 4a-b). These data show that modulating
378 the phosphorylation status of astrocytic ERMs through overexpression of the phospho-
379 dead EZRIN in astrocytes is sufficient to generate synapse number deficits in WT mice,
380 whereas in LRRK2 G2019S$^{ki/ki}$ mice, the same manipulation rescues synapse deficits.
381 These data strongly suggest that the reduction we observed in synapse numbers in the
382 ACC of the LRRK2 G2019S$^{ki/ki}$ mice is largely due to an astrocytic dysfunction caused by
383 the imbalance of ERM phosphorylation. These results also indicate that astrocytes are
384 crucial contributors to excitatory synaptic dysfunction in the LRRK2 G2019S$^{ki/ki}$ mouse
385 cortex.

386 We next investigated whether the same manipulation of adult astrocytes can
387 rescue the inhibitory synapse upregulation in the MOp. We found that neither the WT nor
388 the phospho-dead EZRIN overexpression in adult astrocytes reduced the density of
389 inhibitory synapses back to WT levels in the MOp layer 1 and layer 2/3 of the LRRK2
390 G2019S$^{ki/ki}$ mice (Extended Data Fig. 5c-d). These data suggest that overexpression of
391 phospho-dead EZRIN in adult WT or LRRK2 G2019S$^{ki/ki}$ astrocytes is sufficient to modify
392 the excitatory synapse numbers in the ACC but cannot restore or impair inhibitory
393 synaptic connectivity changes seen in the MOp. It is plausible that LRRK2 G2019S
394 impairs inhibitory synapses in the MOp by altering the number or connectivity of cortical
395 interneurons through a developmental mechanism. Thus, manipulation in the adult is not
396 sufficient to eliminate this phenotype. Future studies on the role of Lrrk2 in cortical
397 development are likely to be beneficial in determining its role in controlling inhibition and
398 how this control is disrupted in PD.

399 Because astrocytic overexpression of phospho-dead EZRIN impacted excitatory
400 synapse numbers in the WT and LRRK2 G2019S$^{ki/ki}$ mice. Next, we performed whole cell
401 patch clamp recordings from the ACC layer 2/3 pyramidal neurons of WT and LRRK2
402 G2019S$^{ki/ki}$ mice transduced with the same AAVs (Extended Data Fig. 5a.
403 Overexpression of WT EZRIN in LRRK2 G2019S$^{ki/ki}$ astrocytes did not rescue the
404 decreased frequency of mEPSCs in the ACC layer 2/3 neurons. However, astrocytic
405 overexpression of the phospho-dead EZRIN significantly reduced the frequency of
406 mEPSCs (reduced by ~54%) in the WT ACC neurons but revamped the frequency of
407 mEPSCs in the LRRK2 G2019S$^{ki/ki}$ ACC neurons (Fig. 4d). Similarly, the cumulative
408 distribution analysis of mEPSCs showed that inter-event interval durations were
409 significantly impacted by astrocytic phospho-dead EZRIN expression in both genotypes
410 in opposite directions (Fig. 4d). In contrast, no significant differences were observed in
411 the mean mEPSC amplitudes across all 4 conditions using posthoc comparisons (Fig.
412 4e).

413 Together, our results reveal that astrocytic overexpression of phospho-dead
414 EZRIN in adult LRRK2 G2019S$^{ki/ki}$ mice can recover the excitatory synapse density and
415 function, whereas the same manipulation disrupts synapse numbers and function in WT
416 ACC neurons. These findings show that the balance of ERM phosphorylation status in
417 astrocytes is crucial for maintaining excitatory synapse density and function in the ACC.
418 This work also reveals a causal link between the astrocytic and synaptic dysfunction
419 induced by the LRRK2 G2019S mutation, providing a non-cell autonomous mechanism
420 for rescuing aberrant cortical wiring in PD pathogenesis.

421 In summary, here we describe a previously unknown role for Lrrk2, a PD-linked
422 gene, in controlling astrocyte morphology and astrocyte-mediated synaptogenic function.
423 Lrrk2 is needed for establishing astrocyte morphological complexity through the
424 phosphorylation of ERMs. LRRK2 G2019S mutation, which increases ERM
425 phosphorylation in astrocytes, also impaired astrocyte morphogenesis *in vitro* and *in vivo*.
426 These findings indicate that ERM phosphorylation balance is critical for the acquisition of
427 complex astrocyte morphology. EZRIN and other ERM proteins are known to interact with
428 cytoskeletal proteins such as F-actin[119] and control the dynamics of F-actin
429 polymerization in a phosphorylation-dependent manner[120]. Future studies investigating
430 how phosphorylated and unphosphorylated states of EZRIN control astrocyte
431 morphogenesis through modulation of the cytoskeleton will be helpful in deciphering
432 mechanisms of astrocyte morphogenesis.

433 LRRK2 G2019S$^{ki/ki}$ mice do not recapitulate cardinal motor symptoms of PD
434 because there is no detectable dopaminergic neuron loss in these mice[67-69]. LRRK2
435 mutation carriers show non-motor symptoms in comparison to non-carriers, such as
436 hyposmia and decreased cognitive performance[150 41,151,152]. These non-motor symptoms
437 arise long before motor dysfunction in PD, indicating that the aberrant synaptic
438 connectivity within multiple brain circuits is present long before the death of the
439 dopaminergic neurons[40-43]. We reasoned that LRRK2 G2019S$^{ki/ki}$ mice may display early
440 circuit dysfunction akin to the non-motor symptoms of prodromal PD. In agreement with
441 this possibility, previous studies showed that LRRK2 G2019S$^{ki/ki}$ mice have deficits in
442 attention and goal-directed learning and differential response to stress[74-76,153]. Our
443 findings showing synaptic deficits in the ACC of LRRK2 G2019S$^{ki/ki}$ mice fit well with these

444 studies because the ACC is a brain region that controls attention, goal-directed actions,
445 and mood[154-159].

446 We observed synaptic deficits in the ACC of LRRK2 G2019S$^{ki/ki}$ mice concurrently
447 with enhanced ERM phosphorylation in astrocytes. Remarkably, overexpression of the
448 phospho-dead EZRIN in the astrocytes of 9-week-old mice can restore the excitatory
449 synapse numbers and function in the ACC layer 2/3 neurons from 12-week-old mice. This
450 result causally links astrocyte dysfunction to the cortical synaptic dysfunction in the
451 LRRK2 G2019S$^{ki/ki}$ mice. Moreover, our findings indicate that restoring astrocyte function,
452 even after development is completed, can be used to treat excitatory synaptic pathology.
453 Future work aimed at understanding the molecular underpinnings of how LRRK2
454 mutations alter synaptogenic functions of astrocytes may lead to effective strategies to
455 treat PD.

456 How does ERM phosphorylation control both the structure and the synaptogenic
457 functions of astrocytes? Astrocytes control synapse formation and function both through
458 cell adhesion and secreted proteins that signal to neurons[31,160]. The canonical function of
459 ERM proteins is linking the actin cytoskeleton with the plasma membrane, thus allowing
460 cellular process outgrowth and morphogenesis[161-163]. Less is known about the roles of
461 ERM in the secretion process. However, it is plausible that ERM phosphorylation
462 regulates synaptogenic protein secretion from astrocytes independent of its roles in
463 astrocyte morphology. Another alternative explanation is a role for astrocytic phospho-
464 ERM proteins in controlling synapse elimination by astrocytes. In agreement with this
465 possibility, a recent study found that synapses are more likely to be eliminated if phospho-
466 ERM proteins were localized to peri-synaptic astrocyte processes in ALS patient brains

467 and mouse models[164]. Future studies investigating LRRK2 and ERM interactomes in
468 astrocytes will help uncover the molecular pathways involved in LRRK2-ERM signaling
469 at the tripartite synapse.

470 In summary, our findings reveal a critical function for LRRK2 in astrocyte
471 development and how LRRK2 G2019S mutation derails important roles of astrocytes in
472 maintaining synaptic connectivity in the developing and mature cortex. Furthermore, here
473 we pinpoint the regulation of astrocytic ERM phosphorylation as a molecular mechanism
474 that is impaired when LRRK2 G2019S mutation is present in astrocytes. These findings
475 suggest that LRRK2-mediated ERM phosphorylation is an early mediator of PD
476 pathogenesis in astrocytes and that astrocytes can be directly responsible for synaptic
477 dysfunction seen in the early stages of PD.

478

479 **METHODS**

480 **Animals:**

481 All mice and rats were used in accordance with the Institutional Animal Care and Use
482 Committee (IACUC) and the Duke Division of Laboratory Animal Resources (DLAR)
483 oversight (IACUC Protocol Numbers A147-17-06 and A117-20-05). All mice and rats were
484 housed under typical day/night conditions of 12-hour cycles. LRRK2 G2019S$^{ki/ki}$ mice
485 (RRID: IMSR_TAC:13940) were obtained through Taconic. Aldh1l1-EGFP (RRID:
486 MMRRC_011015-UCD) mice were obtained through MMRRC. Wild-type CD1 mice used
487 for PALE were purchased through Charles River Laboratories (RRID:
488 IMSR_CRL:022). LRRK2 G2019S-BAC Transgenic rats (RRID: IMSR_TAC:10681) were
489 obtained through Taconic. LRRK2 knock-out rats (RRID: RGD_7241056) were obtained
490 through SAGE Labs, Inc. in St. Louis, MO.

491 Mice and rats were used for experiments as specified in the text and figure legends.
492 For all experiments, age, and sex-matched mice were randomly assigned to experimental
493 groups based on genotypes. For MLi-2 treatment of astrocytes, only female rat astrocyte
494 cultures were used for Western blot and analysis because male rat astrocyte cultures
495 have low phospho-ERM levels *in vitro*. For other experiments, mice of both sexes were
496 included in the analysis, and we did not observe any influence or association of sex on
497 the experimental outcomes.

498 **Primary cortical neuron isolation and culture:**

499 Purified (glia-free) rat cortical neurons were prepared as described previously[28]. Briefly,
500 cortices from P1 rat pups of both sexes (Sprague Dawley, Charles River Laboratories,
501 SD-001) were micro-dissected, digested in papain (~7.5 units/ml) at 33°C for 45 minutes,

502 triturated in low and high ovomucoid solutions, resuspended in panning buffer (DPBS
503 (GIBCO 14287) supplemented with BSA and insulin) and passed through a 20 μm mesh
504 filter (Elko Filtering 03-20/14). Filtered cells were incubated on negative panning dishes
505 coated with Bandeiraea Simplicifolia Lectin 1 (x2), followed by goat anti-mouse IgG+IgM
506 (H+L) (Jackson ImmunoResearch 115-005-044), and goat anti-rat IgG+IgM (H+L)
507 (Jackson ImmunoResearch 112-005-044) antibodies, then incubated on positive panning
508 dishes coated with mouse anti-L1 (ASCS4, Developmental Studies Hybridoma Bank,
509 Univ. Iowa) to bind cortical neurons. Adherent cells were collected by forceful pipetting
510 with a P1000 pipette. Isolated neurons were pelleted (11 minutes at 200 g) and
511 resuspended in serum-free neuron growth media (NGM; Neurobasal, B27 supplement,
512 2 mM L-Glutamine, 100 U/ml Pen/Strep, 1 mM sodium pyruvate, 4.2 μg/ml Forskolin,
513 50 ng/mL BDNF, and 10 ng/mL CNTF). 70,000 neurons were plated onto 12 mm glass
514 coverslips coated with 10 μg/ml poly-D-lysine (PDL, Sigma P6407) and
515 2 μg/ml laminin and incubated at 37°C in 10% CO_2. On day *in-vitro* (DIV) 2, half of the
516 media was replaced with NGM Plus (Neurobasal Plus, B27 Plus, 100 U/mL Pen/Strep,
517 1 mM sodium pyruvate, 4.2 μg/ml Forskolin, 50 ng/ml, BDNF, and 10 ng/ml CNTF) and
518 AraC (10 μM) was added to stop the growth of proliferating contaminating cells. On DIV
519 3, all the media was replaced with NGM Plus. In experiments involving lentivirus infection,
520 100 μl of supernatant containing lentivirus plus polybrene (1 μg/ml) was added to the
521 AraC NGM mixture on DIV 2 and completely washed out on DIV 3 and replaced with NGM
522 Plus containing 100 ng/ml BDNF. Neurons were fed on DIV 6 and DIV 9 by replacing half
523 of the media with NGM Plus.

524 **Primary cortical astrocyte isolation and culture:**

525 Rat cortical astrocytes were prepared as described previously[28]. P1 rat cortices from both
526 sexes were micro-dissected, papain digested, triturated in low and high ovomucoid
527 solutions, and resuspended in astrocyte growth media (AGM: DMEM (GIBCO 11960), 10%
528 FBS, 10 μM, hydrocortisone, 100 U/ml Pen/Strep, 2 mM L-Glutamine, 5 μg/ml Insulin,
529 1 mM Na Pyruvate, 5 μg/ml N-Acetyl-L-cysteine). Between 15-20 million cells were plated
530 on 75 mm^2 flasks (non-ventilated cap) coated with poly-D-lysine and incubated at 37°C
531 in 10% CO_2. On DIV 3, the removal of non-astrocyte cells was performed by forcefully
532 shaking closed flasks by hand for 10-15 s until only an adherent monolayer of astrocytes
533 remained. AraC was added to the media from DIV 5 to DIV 7 to eliminate contaminating
534 fibroblasts. On DIV 7, astrocytes were trypsinized (0.05% Trypsin-EDTA) and plated into
535 12-well or 6-well dishes. On DIV 8, cultured rat astrocytes were transfected
536 with shRNA and/or expression plasmids using Lipofectamine LTX with Plus Reagent
537 (Thermo Scientific) per the manufacturer's protocol. Briefly, 1 μg (12-well) or 2 μg (6-well)
538 total DNA was diluted in Opti-MEM containing Plus Reagent, mixed with Opti-MEM
539 containing LTX (1:2 DNA to LTX), and incubated for 30 minutes. The transfection solution
540 was added to astrocyte cultures and incubated at 37°C for 3 hours. On DIV 10, astrocytes
541 were trypsinized, resuspended in NGM plus, plated (20,000 cells per well) onto DIV 10
542 neurons, and co-cultured for 48 hours.

543 **shRNA plasmids:**

544 pLKO.1 Puro plasmids containing shRNA (pLKO.1-shRNA) against
545 mouse/rat *Lrrk2* (sh*Lrrk2*: TRCN0000322193; GGCCGAGTTGTGGATCATATT), was
546 obtained from the RNAi Consortium (TRC) via Dharmacon. A scrambled shRNA
547 sequence was generated (GTTGCTGAATGGCGGATCTAT) and cloned into the pLKO.1

548 TRC cloning vector[165] according to Addgene protocols
549 (https://www.addgene.org/protocols/plko/). To generate pLKO.1 shRNA plasmids that
550 express EGFP (pLKO.1-shRNA-EGFP), CAG-EGFP was removed from pLenLox-shNL1-
551 CAG-EGFP[166] and inserted between Kpn1 and SpeI sites in pLKO.1 Puro, replacing
552 the puromycin resistance gene. pLKO.1 shRNA mCherry plasmids were generated by
553 replacing EGFP with mCherry between KpnI and NheI sites.

554 **PiggyBac plasmids:**

555 pPB-CAG-EGFP and pGLAST-PBase were a gift from Dr. Joseph Loturco[167]. To generate
556 pPB-CAG-mCherry-CAAX, mCherry-CAAX was inserted between XmaI and NotI
557 restrictions sites to replace EGFP. To insert the hU6 promoter and shRNA in pPB-CAG-
558 mCherry-CAAX, a DNA fragment containing hU6 and shRNA was amplified from pLKO.1-
559 shRNA using Phusion High-Fidelity DNA Polymerase (NEB) with primers that introduced
560 SpeI restriction sites (Forward Primer: GGACTAGTCAGGCCCGAAGGAATAGAAG;
561 Reverse Primer: GGACTAGTGCCAAAGTGGATCTCTGCTG). PCR products were
562 purified, digested with SpeI, and ligated into pPBCAG-mCherry-CAAX at the SpeI
563 restriction site. An analytical digest with EcoRI followed by sequencing was used to
564 confirm the orientation of the inserted DNA fragment.

565 **Ezrin plasmids:**

566 pZac2.1-GfaABC1D-Lck-GCaMP6f was a gift from Dr. Baljit Khakh (Addgene plasmid
567 #52924). pZac2.1-GfaABC1D-BioID2-HA was generated by PCR of BioID2 from pAAV-
568 hSyn-BioID2-Linker-Synapsin1a-HA[168] (primers Fw: 5'-
569 ctagcctcgagaattcaccatgttcaaaaatcttatttg-3', Rv: 5'-ccgggtcgactctagatgcgtaatccggtacatcg-

570 3') and insertion into the EcoRI and XbaI restriction sites of pZac2.1-GfaABC1D-Lck-
571 GCaMP6f using In-Fusion cloning (TaKaRa). pHJ421(pEGFP-Ezrin WT) and pHJ423
572 (pEGFP-Ezrin T567D) were a gift from Stephen Shaw (Addgene plasmid # 20680 and #
573 20681). pZac2.1-GfaABC1D-Ezrin WT-BioID2-HA and pZac2.1-GfaABC1D-Ezrin
574 T567D-BioID2-HA were generated by PCR of Ezrin from pHJ421 or pHJ423 (primers Fw:
575 5'-ctagcctcgagaattcaccatgccgaaaccaatca-3', Rv: 5'-
576 tgaacatggtgaattccgacagggcctcgaactcg-3') and insertion into the EcoRI restriction sites of
577 pZac2.1-GfaABC1D-BioID2, respectively. To generate pZac2.1-GfaABC1D-Ezrin
578 T567A-BioID2-HA plasmid, Q5® Site-Directed Mutagenesis Kit (NEB) was used with
579 mutagenesis primers (Fwd: CAAGTACAAGGCGCTGCGGCAGA; Rev:
580 TCCCGGCCTTGCCTCATG)

581 **Lentivirus production and transduction:**

582 Lentiviruses containing shRNA targeting vectors were produced to test the knockdown
583 efficiency of shRNA constructs in cultured primary astrocytes or to bulk transduce
584 neurons with shRNA and GFP. To produce lentivirus, HEK293T cells were transfected
585 with a pLKO.1 shRNA Puro targeting plasmid (for astrocyte transduction), an envelope
586 plasmid (VSVG), and a packaging plasmid (dR8.91) using X-tremeGENE (Roche). One
587 day after transfection, the media was replaced with AGM (for astrocyte transduction), and
588 media containing lentivirus was collected on days 2 and 3 post-transfection. To assess
589 the knockdown efficiency of shRNAs in astrocytes, rat primary astrocytes at DIV 7 were
590 plated in 6-well dishes in 2 ml of AGM. On DIV 8, 1 ml of AGM was removed, and 500 µl
591 of fresh AGM was added along with 500 µl of lentivirus-containing media and 1 µg/ml
592 polybrene. Cultured astrocytes were treated with puromycin (1 µg/ml) from DIV 10-15 to

593 select for transduced cells. Cultured astrocytes were lysed at DIV 15 for protein extraction
594 and Western blot analysis.

595 **MLi-2 treatment of astrocytes:**

596 Cortical astrocytes were isolated from P0-P1 rat female pups as described in the "Cortical
597 astrocyte isolation and culture" section. Cultured astrocytes were treated with 0, 30, and
598 100 nM LRRK2 kinase inhibitor, MLi-2 (Tocris; Catalog number: 5756), for 72 hours.
599 Cultured astrocytes were lysed at DIV 11 for protein extraction and Western blot analysis.

600 **Protein extraction and Western blotting:**

601 Protein was extracted from cultured rat astrocytes using membrane solubilization buffer
602 (25 mM Tris pH 7.4, 150 mM NaCl, 1 mM $CaCl_2$, 1 mM $MgCl_2$, 0.5% NP-40, and protease
603 inhibitors). Cultured astrocytes were washed twice with ice-cold TBS containing 1 mM
604 $CaCl_2$ and 1 mM $MgCl_2$ and incubated on ice in membrane solubilization buffer for
605 20 minutes with occasional agitation. Cell lysates were collected, vortexed briefly, and
606 centrifuged at 4°C at high speed for 10 minutes to pellet non-solubilized material. The
607 supernatant was collected and stored at −80°C.

608 Pierce BSA Protein Assay Kit (Thermo Fisher) was used to determine protein
609 concentration, and lysates were mixed with 4x Pierce™ Reducing Sample Buffer (Thermo
610 Scientific) and incubated at 45°C for 45 minutes to denature proteins. 7-10 µg (cultured
611 astrocyte lysates) of protein was loaded into Bolt™ 4–12% Bus-Tris Plus gels (Thermo
612 Scientific) and run at 150 V for 1 hour. Proteins were transferred at 100 V to PVDF
613 membrane (Millipore) for 1.5 hours, blocked in 5% BSA in TBST (137 mM NaCl, 2.68 mM
614 KCl, 24.7 mM Tris-Base, 0.1% (w/v) Tween 20) for 1 hour and incubated in primary

615 antibodies overnight at 4°C. Primary antibodies used were: anti-LRRK2 (Rabbit, 1:500;
616 ab133474, abcam), GAPDH (mouse, 1:5000; ab8245, abcam), β-actin (mouse, 1:5000;
617 A5441, Millipore Sigma), phospho-ERM (Rabbit, 1:500; #3141, Cell Signaling), ERM
618 (Rabbit, 1:500; #3142, Cell Signaling), phospho-Rab10 (Rabbit, 1:500; ab230261,
619 abcam), Rab10 (Rabbit, 1:500; ab237703, abcam). The next day, membranes were
620 washed with TBST, incubated in HRP secondary antibodies (Thermo Fisher Scientific)
621 for 2 hours, washed in TBST, and imaged on a Biorad Gel Doc imaging system. Protein
622 levels were quantified using FIJI.

623 **Immunocytochemistry:**

624 Astrocyte-neuron co-cultures on glass coverslips were fixed on DIV 12 with warm 4%
625 PFA for 7 minutes, washed 3 times with PBS, blocked in a blocking buffer containing 50%
626 normal goat serum (NGS) and 0.4% Triton X-100 for 30 minutes, and washed in PBS.
627 Samples were then incubated overnight at 4°C in primary antibodies diluted in blocking
628 buffer containing 10% NGS, washed with PBS, incubated in Alexa Fluor conjugated
629 secondary antibodies (Life Technologies) for 2 hours at room temperature, and washed
630 again in PBS. Coverslips were mounted onto glass slides (VWR Scientific) with
631 Vectashield mounting media containing DAPI (Vector Labs), sealed with nail polish, and
632 imaged on an AxioImager M1 (Zeiss) fluorescence microscope. Images of healthy
633 astrocytes with strong expression of fluorescent markers that did not overlap with other
634 fluorescent astrocytes were acquired at 40x magnification in red, green, and/or DAPI
635 channels using a CCD camera. Astrocyte morphological complexity was analyzed in FIJI
636 using the Sholl analysis plugin[169], as described previously[28] (https://github.com/Eroglu-
637 Lab/In-Vitro-Sholl). Statistical analyses were conducted using a custom code in R

638 (https://github.com/Eroglu-Lab/In-Vitro-Sholl). A mixed-effect model with multiple
639 comparisons made using the Tukey post-test was used for Sholl analysis to account for
640 the variability per experiment as a random effect to evaluate differences between the
641 conditions. The exact number of independent experiments and the exact number of cells
642 analyzed are indicated in the figure legend for each experiment. To ensure the health of
643 astrocyte-neuron co-cultures, the peak for the number of astrocyte intersections must be
644 greater than or equal to 25 in the control condition. We imaged non-overlapping
645 astrocytes that contained a single nucleus (DAPI stain) and expressed consistent
646 fluorescent markers and EZRIN constructs according to the experimental conditions.

647 **Postnatal astrocyte labeling by electroporation (PALE):**

648 Late P0/early P1 mice were sedated by hypothermia until anesthetized, and 1 µl
649 of plasmid DNA mixed with Fast Green Dye was injected into the lateral ventricle of one
650 hemisphere using a pulled glass pipette (Drummond). For shRNA knockdown
651 experiments in wild-type CD1 mice, the 1 µl of DNA contained 1 µg of pGLAST-PBase
652 and 1 µg of pPB-shRNA-mCherryCAAX was injected. To label astrocytes in WT
653 and LRRK2 G2019S$^{ki/ki}$ mice, the 1 µl of DNA contained 1 µg of pGLAST-PBase and 1
654 µg of pPB-mCherry-CAAX was injected per mouse.

655 For PALE-mediated overexpression of phospho-mimetic EZRIN in shRNA knockdown
656 experiments, 0.5 µg pGLAST-PBase, 0.5 µg pPB-shRNA-mCherryCAAX, and 1 µg
657 pZac2.1-GfaABC1D-Ezrin T567D-BioID2-HA were injected in a total volume of 1 µl. For
658 phospho-dead EZRIN overexpression in WT and LRRK2 G2019S$^{ki/ki}$ mice, 0.5 µg
659 pGLAST-PBase, 0.5 µg of pZac2.1-gfaABC1D-mCherry-CAAX and 1 µg of pZac2.1-
660 GfaABC1D-Ezrin T567A-BioID2-HA were injected in a total volume of 1 µl. Following DNA

661 injection, electrodes were oriented with the positive terminal above the frontal cortex and
662 the negative terminal below the chin, and 5 discrete 50 ms pulses of 100 V spaced
663 950 ms apart were applied. Pups were recovered on a heating pad, returned to their home
664 cage, and monitored until collection at P21. The number of mice used for each experiment
665 is indicated in the figure legends. All animals appeared healthy at the time of collection.
666 Brain sections were examined for the presence of electroporated cells before staining.

667 **Adeno-associated virus (AAV) production and administration:**

668 Purified AAVs were produced as described previously[170]. Briefly, HEK293T cells were
669 transfected with pAd-DELTA F6, serotype plasmid AAV PHP.eB, and AAV plasmid
670 (pZac2.1-GfaABC1D-Ezrin-BioID2-HA or pZac2.1-GfaABC1D-Ezrin T567A-BioID2-HA).
671 Three days after transfection, cells were collected in 15 mM NaCl, 5 mM Tris-HCl, pH 8.5,
672 and lysed with repeat freeze-thaw cycles followed by treatment with Benzonase (Novagen
673 70664) at 37°C for 30 minutes. Lysed cells were pelleted by centrifugation, and the
674 supernatant, containing AAVs, was applied to an Optiprep density gradient (Sigma D1556,
675 15%, 25%, 40%, and 60%) and centrifuged at 67,000 rpm using a Beckman Ti-70 rotor
676 for 1 hour. The AAV-enriched fraction was isolated from between 40% and
677 60% iodixanol solution and concentrated by repeated washes with sterile PBS in an
678 Amicon Ultra-15 filtration unit (NMWL: 100 kDa, Millipore UFC910008) to a final volume
679 of ~100 µl and aliquoted for storage at −80°C. 9-week-old WT or LRRK2 G2019S$^{ki/ki}$ mice
680 placed in a stereotaxic frame were anesthetized through inhalation of 1.5% isofluorane
681 gas. 10 µl of purified AAVs having a titer of ~1 x 10^{12} GC/ml was introduced into the
682 mouse brain intravenously by injection into the retro-orbital sinus. After 3 weeks at 12-
683 week-old, mice were anesthetized with 200 mg/kg Tribromoethanol (Avertin) and

684 transcardially perfused with TBS/Heparin and 4% paraformaldehyde (PFA) at room
685 temperature (RT). Harvested brains were post-fixed overnight in 4% PFA, cryoprotected
686 in 30% sucrose, and the brain blocks were prepared with O.C.T. (TissueTek) to store at
687 −80°C. 30 µm thick brain sections were obtained through cryosectioning using a Leica
688 CM3050S (Leica, Germany) vibratome and stored in a mixture of TBS and glycerol at
689 −20°C for further free-float antibody staining procedures.

690 **Immunohistochemistry on mouse brain sections:**

691 Mice used for immunohistochemistry were anesthetized with 200 mg/kg Avertin and
692 perfused with TBS/Heparin and 4% PFA. Brains were collected and post-fixed in 4% PFA
693 overnight, cryoprotected in 30% sucrose, frozen in a solution containing 2 parts 30%
694 sucrose and 1-part O.C.T. (TissueTek), and stored at −80°C. Floating coronal tissue
695 sections of 30 µm, 40 µm or 100 µm thickness were collected and stored in a 1:1 mixture
696 of TBS/glycerol at −20°C. For immunostaining, sections were washed in 1x TBS
697 containing 0.2% Triton X-100 (TBST), blocked in 10% NGS diluted in TBST, and
698 incubated in primary antibody for 2-3 nights at 4°C with gentle shaking. Primary antibodies
699 used were anti-LRRK2 (Rabbit, 1:500; ab133474, Abcam), phospho-ERM (Rabbit, 1:500;
700 #3141, Cell Signaling), Sox9 (Rabbit, 1:500; AB5535, Millipore), GFAP (Rabbit, 1:500;
701 Z0334, Agilent DAKO), VGluT1 (Guinea pig, 1:2000; 135304, Synaptic Systems), PSD95
702 (Rabbit, 1:300; 51-6900, Invitrogen), VGAT (Guinea pig, 1:1000; 131004, Synaptic
703 Systems), and GEHPYRIN (Rabbit, 1:1000; #14304S, Cell Signaling). Following the
704 primary incubation, sections were washed in TBST, incubated in Alexa Fluor conjugated
705 secondary antibodies diluted 1:200 (Life Technologies) for 2-3 hours at room temperature,
706 washed with TBST, and mounted onto glass slides using a homemade mounting media

707 (90% Glycerol, 20 mM Tris pH 8.0, 0.5% n-Propyl gallate) and sealed with nail polish. For
708 DAPI staining, DAPI (1:50,000) was added to the secondary antibody solution for the final
709 10 minutes of incubation. Images were acquired with an Olympus FV 3000 microscope.

710 **Mouse astrocyte territory volume analysis:**

711 To assess the territory volume of individual astrocytes in the mouse cortex, 100 µm-thick
712 floating sections containing anterior cingulate cortex (ACC) and primary motor cortex
713 (MOp) astrocytes labeled sparsely via PALE with mCherry-CAAX were collected. High-
714 magnification images containing an entire astrocyte (50-60 µm z-stack) were acquired
715 with an Olympus FV 3000 microscope with the 60x objective. Criteria for data inclusion
716 required that the entirety of the astrocyte could be captured within a single brain section
717 and that the astrocyte was in layer 2/3 of the ACC or MOp. Astrocytes in which the entire
718 astrocyte could not be captured within the section or was in other layers or outside of the
719 ACC or MOp were not imaged. Imaged astrocytes were analyzed using Imaris Bitplane
720 software as described previously[28]. Briefly, surface reconstructions were generated, and
721 the Imaris Xtensions "Visualize Surface Spots" and "Convex Hull" were used to create an
722 additional surface render representing the territory of the astrocyte. The volume of each
723 territory was recorded, and astrocyte territory sizes from biological replicates were
724 analyzed across experimental conditions using a nested two-way ANOVA followed by
725 Bonferroni posthoc test. For 3D Sholl analysis of individual PALE astrocytes, we first
726 loaded images onto Imaris and then created a surface. After generating the surface of
727 astrocytes, we created filaments using 'Add new filament (leaf icon)'. For the
728 quantification of complexity, we clicked on the gear tool on Imaris to display Sholl

729 intersections. The number of animals and cells/animals analyzed are specified in the
730 figure legend for each experiment.

731 **Mouse synapse imaging and analysis:**

732 Staining, image acquisition, and analysis of synaptic density were performed as described
733 previously[28,171] with slight adjustments. Synaptic staining was performed in coronal
734 sections (30 µm thick) containing the ACC and MOp from WT and LRRK2 G2019S$^{ki/ki}$
735 mice. To label pre and postsynaptic proteins, the following antibody combinations were
736 used: VGluT1 and PSD95 (excitatory, intracortical), VGAT, and GEPHYRIN (inhibitory).
737 High magnification 60x objective plus 1.64x optical zoom z-stack images containing 15
738 optical sections spaced 0.34 µm apart were obtained using an Olympus FV 3000 inverted
739 confocal microscope. Each z-stack was converted into 5 maximum projection images
740 (MPI), each corresponding to a 1 µm section of z plane, by using FIJI. Synapses were
741 identified by the colocalization of pre and postsynaptic puncta. The number of co-localized
742 synaptic puncta of excitatory intracortical (VGluT1/PSD95) and inhibitory
743 (VGAT/GEPHYRIN) synapses were obtained using the FIJI plugin Puncta Analyzer[147].
744 15 MPIs were analyzed for each mouse (5 MPI/tissue section, 3 tissue sections/mouse).
745 Between 4 and 5, age and sex-matched mice/genotype/condition were analyzed for each
746 synaptic staining combination, as indicated in the figure legends. All animals appeared
747 healthy at the time of collection. No data were excluded.

748 **Cell counting, imaging, and analysis:**

749 Tile scan images containing the anterior cingulated cortex (ACC) and primary motor
750 cortex (MOp) from P21 WT and LRRK2 G2019S$^{ki/ki}$; Aldh1l1-eGFP mice were acquired

751 on a confocal Leica SP8 STED microscope using the galvo scanner and 20x objective.
752 For ALDH1L1-EGFP and SOX9 double positive cell counting in the ACC and MOp, the
753 cells labeled with ALDH1L1-EGFP and SOX9 were counted by hand using the cell
754 counter tool in FIJI. 2-4 sections per brain from 3 sex and age-matched mice/genotype
755 were analyzed.

756 **Human brain section staining:**

757 Floating human frontal cortex sections of 40 µm thickness were obtained from Banner
758 Sun Health Research Institute in Sun City, Arizona (4 control and 3 LRRK2 G2019S
759 mutation carrier subjects). None of the control subjects had a history of dementia or
760 neurological or psychiatric disorders at the time of death (See Supplemental Table 1).
761 Informed and written consent was obtained from the donors. For immunostaining,
762 sections were washed in 1x TBS containing 0.3% Triton X-100 (TBST), blocked in 3%
763 NGS diluted in TBST, and incubated in primary antibody 2-3 nights at 4°C with shaking.
764 Primary antibodies used were GFAP (chicken, 1:250; AB5541, Millipore Sigma) and
765 phospho-ERM (Rabbit, 1:250; #3726, Cell Signaling). Following primary incubation,
766 sections were washed in TBST, incubated in Alexa Fluor conjugated secondary
767 antibodies diluted 1:200 (Life Technologies) for 2-3 hours at room temperature, washed
768 with TBST, and mounted onto glass slides using a homemade mounting media (90%
769 Glycerol, 20 mM Tris pH 8.0, 0.5% n-Propyl gallate) and sealed with nail polish.

770 **Mouse brain slice electrophysiology:**

771 For whole-cell patch-clamp recordings, 3-4 mice of each genotype and condition were
772 used for miniature excitatory postsynaptic current (mEPSC) and miniature inhibitory

773 postsynaptic current (mIPSC) measurements. WT and *LRRK2* G2019S$^{ki/ki}$ mice of both
774 sexes were anesthetized with 200 mg/kg tribromoethanol (avertin) and decapitated. After
775 decapitation, the brains were immersed in ice-cold artificial cerebrospinal fluid (aCSF, in
776 mM): 125 NaCl, 2.5 KCl, 3 mM $MgCl_2$, 0.1 mM $CaCl_2$, 10 glucose, 25 $NaHCO_3$, 1.25
777 $NaHPO_4$, 0.4 L-ascorbic acid, and 2 Na-pyruvate, pH 7.3-7.4 (310 mOsmol). 350 µm thick
778 coronal slices containing the ACC were obtained using a vibrating tissue slicer (Leica
779 VT1200; Leica Biosystems). Slices were immediately transferred to standard aCSF (33°C,
780 continuously bubbled with 95% O_2 – 5% CO_2) containing the same as the low-calcium
781 aCSF but with 1 mM $MgCl_2$ and 1-2 mM $CaCl_2$. After 30-minute incubation at 33°C, slices
782 were transferred to a holding chamber with the same extracellular buffer at room
783 temperature (RT: ~25°C). Brain slices were visualized by an upright microscope (BX61WI,
784 Olympus) through a 40x water-immersion objective equipped with infrared-differential
785 interference contrast optics in combination with a digital camera (ODA-IR2000WCTRL).
786 Patch-clamp recordings were performed by using an EPC 10 patch-clamp amplifier,
787 controlled by Patchmaster Software (HEKA). Data were acquired at a sampling rate of 50
788 kHz and low-pass filtered at 6 kHz.

789 To measure mEPSCs, the internal solution contained the following (in mM): 125 K-
790 gluconate, 10 NaCl, 10 HEPES, 0.2 EGTA, 4.5 MgATP, 0.3 NaGTP, and 10 Na-
791 phosphocreatine, pH adjusted to 7.2 – 7.4 with KOH and osmolality set to ~ 300 mOsmol.
792 mEPSCs were measured in the aCSF bath solution containing 1 µM tetrodotoxin and 50
793 µM Picrotoxin at -70 mV in voltage-clamp mode. To measure mIPSCs, the internal
794 solution contained the following (in mM): 77 K-gluconate, 77 KCl, 10 HEPES, 0.2 EGTA,
795 4.5 MgATP, 0.3 NaGTP, and 10 Na-phosphocreatine, pH adjusted to 7.2 – 7.4 with KOH

796 and osmolality set to ~ 300 mOsmol. mIPSCs were measured in the aCSF bath solution
797 containing 1 μM tetrodotoxin and 10 μM 6-cyano-7-nitroquinoxaline-2,3- dione (CNQX),
798 and 50 μM D-2-amino-5-phosphonopentanoate (D-AP5) at -70 mV in voltage-clamp
799 mode. mEPSCs and mIPSCs recorded at -70 mV were detected using Minhee Analysis
800 software (https://github.com/parkgilbong/Minhee_Analysis_Pack). To analyze the
801 frequency, events were counted over 5 minutes of recording. To obtain the average
802 events for each cell, at least 100 non-overlapping events were detected and averaged.
803 The peak amplitude of the average mEPSCs was measured relative to the baseline
804 current.

805 **Quantification and statistical analysis:**

806 All statistical analyses were performed in GraphPad Prism 9. Exact value of n, what n
807 represents, and specific statistical tests for each experiment are indicated in the figure
808 legend for each experiment. All data are represented as mean ± standard error of the
809 mean, and data points are shown where applicable. Exact *P*-values are listed in the figure
810 for each experiment. Where indicated, the unpaired two-tailed t-tests were run using
811 Welch`s correction, and a correction for multiple comparisons was applied using Hom-
812 Sidak method with an alpha threshold of 0.05 for adjusted *P*-value. A Geisser-
813 Greenhouse correction was used for both One-way and Two-way ANOVA analyses. For
814 Sholl analysis, statistical analyses were conducted using a custom code in R
815 (https://github.com/Eroglu-Lab/In-Vitro-Sholl). A mixed-effect model with multiple
816 comparisons made using the Tukey post-test was used for Sholl analysis to account for
817 the variability per experiment as a random effect to evaluate differences between the
818 conditions. Sample sizes were determined based on previous experience for each

819 experiment to yield high power to detect specific effects. No statistical methods were used
820 to predetermine the sample size. All experimental animals that appeared healthy at the
821 time of tissue collection were processed for data collection.

822 **Acknowledgments:**

823 We thank Drs. Nicole Calakos, Katja Brose, Andrew Singleton, Dolores Irala, Francesco
824 P. Ulloa Severino, Juan Ramirez, Justin T. Savage, Gabrielle Séjourné, and other Eroglu
825 lab members for critical feedback about the manuscript. We thank Adam Okinaga and
826 Donna Porter for excellent technical help. This work was supported by a Foerster
827 Bernstein Women In STEM Postdoctoral Fellowship to SW, and a Chan Zuckerberg
828 Initiative, Neurodegeneration Challenge Network Collaborative grant (2018-191999 and
829 DAF2021-237435) to CE and ARLS, and by the N.I.H. grants R35-NS122140 to A.R.L.S.
830 and R01-NS102237 to CE, and by the Michael J. Fox Foundation for Parkinson's Research
831 (MJFF) Astrocyte Biology in PD pilot grant (MJFF 17914 to CE and ARLS), and by the
832 joint efforts of MJFF and the Aligning Science Across Parkinson's (ASAP) initiative. MJFF
833 administers the grant [ASAP-020607 to CE and SHS] on behalf of ASAP and itself
834 Michael J Fox Foundation. Dr. Cagla Eroglu is an HHMI Investigator. We are grateful to
835 the Banner Sun Health Research Institute Brain and Body Donation Program of Sun City,
836 Arizona for the provision of human biological materials. The Brain and Body Donation
837 Program has been supported by the National Institute of Neurological Disorders and
838 Stroke (U24 NS072026 National Brain and Tissue Resource for Parkinson's Disease and
839 Related Disorders), the National Institute on Aging (P30AG19610 and P30AG072980,
840 Arizona Alzheimer's Disease Center), the Arizona Biomedical Research Commission
841 contracts 4001, 0011, 05-901 and 1001 to the Arizona Parkinson's Disease Consortium)
842 and the Michael J. Fox Foundation for Parkinson's Research.

843 **IP rights notice**

844 This article is subject to HHMI's Open Access to Publications policy. HHMI lab heads
845 have previously granted a nonexclusive CC BY 4.0 license to the public and a
846 sublicensable license to HHMI in their research articles. Pursuant to those licenses, the
847 author-accepted manuscript of this article can be made freely available under a CC BY
848 4.0 license immediately upon publication.

849 **Author contributions**

850 Conceptualization, SW, ARLS, and CE; Methodology, SW, DSB, CXT, TT, MPR, KD,
851 SHS, and CE; Investigation, SW, DSB, CXT, KD; Formal analysis, SW, CXT, and MPR;
852 Resources, KS; Writing – original draft, SW and CE; Writing – Review & Editing, SW,
853 SHS, CXT, TT, MPR, KD, KS, ARLS, DSB, and CE; Funding Acquisition, SW, SHS, ARLS,
854 and CE.

855 **Declaration of interests**

856 The authors declare no competing interests.

857 **Data Availability**

858

859 The data that support the findings of this study are available from the corresponding
860 author (Dr. Cagla Eroglu) upon request after the publication of this manuscript. The data
861 include experiment records, raw data, and analysis. The authors confirm that all data
862 underlying the findings will be made fully available without restriction upon publication.

863 **Code availability**

864 The code used to analyze Sholl data is available on the link https://github.com/Eroglu-
865 Lab/Sholl_Macro.

866 **FIGURE LEGENDS**

867 **Figure 1. Astrocytic LRRK2 controls astrocyte morphology by balancing ERM**
868 **phosphorylation levels *in vitro*. a,** Schematic of astrocyte-neuron co-culture assay. **b,**
869 (Upper) Rat cortical astrocytes transfected with scrambled shRNA (shControl-GFP) or
870 shRNA targeting LRRK2 (sh*Lrrk2*-GFP) and LRRK2 knockout (KO) rat cortical astrocytes
871 co-cultured with wild-type cortical neurons. Scale bar, 10 μm. (Lower) Quantification of
872 astrocyte branching complexity. n = 56 (shControl-GFP), 54 (sh*Lrrk2*-GFP), 52 (LRRK2
873 KO) astrocytes co-cultured with wild-type (WT) cortical neurons compiled from three
874 independent experiments. We fitted a linear mixed model with the number of intersections
875 as an outcome variable, condition as a predictor, and the number of cells and cell radius
876 were entered as random effects. Within this model, sh*Lrrk2* (beta = 5.91, t(171) = 12.59)
877 and LRRK2 KO (beta = 5.43, t(171) = 11.28) led to a significant decrease of number of
878 intersections compared to shControl (beta = 12.37, t(171) = 25.72). Tukey multiple
879 comparisons test revealed a significant difference between shControl-GFP and LRRK2
880 KO ($p < 0.001$) and between shControl-GFP and sh*Lrrk2*-GFP ($p < 0.001$). Tukey multiple
881 comparisons test revealed no difference between sh*Lrrk2*-GFP and LRRK2 KO ($p =$
882 0.7579). **c,** WT or LRRK2 G2019S rat cortical astrocytes transfected with GFP and co-
883 cultured with WT cortical neurons or LRRK2 G2019S cortical neurons. Scale bar, 10 μm.
884 **d,** Quantification of astrocyte branching complexity. n = 61 (WT), 61 (LRRK2 G2019S)
885 astrocytes co-cultured with WT cortical neurons compiled from three independent
886 experiments. n = 41 (WT), 40 (LRRK2 G2019S) astrocytes co-cultured with LRRK2
887 G2019S cortical neurons compiled from two independent experiments. We fitted a linear
888 mixed model with number of intersections as outcome variable, condition as predictor and

889 number of cells and cell radius were entered as random effects. Within this model, LRRK2
890 G2019S (beta = 7.55, t(113) = 18.95) led to a significant decrease of number of
891 intersections compared to WT astrocytes (beta = 10.86, t(113) = 28.47). WT (beta = 7.12,
892 t(152) = 15.44) and LRRK2 G2019S (beta = 6.49, t(152) = 13.72) astrocytes co-cultured
893 on LRRK2 G2019S neurons led to a significant decrease of number of intersections
894 compared to WT astrocytes co-cultured with WT neurons (beta = 14.42, t(152) = 30.09).
895 Tukey multiple comparisons test revealed no difference between WT and LRRK2 G2019S
896 astrocytes co-cultured on LRRK2 G2019S neurons (p = 0.7696). Tukey multiple
897 comparisons test revealed a significant difference between WT and LRRK2 G2019S
898 astrocytes co-cultured on WT neurons (p = 1.99E-09). **e,** WT astrocytes treated with
899 DMSO, 30 nM MLi-2, or 100 nM MLi-2 were lysed and subjected to Western blotting.
900 Western blotting was performed using phospho-ERM, ERM, phospho-Rab10, and Rab10
901 antibodies. Results are representative of 4 independent experiments. **f,** Densitometric
902 analysis of phospho-ERM levels in **Fig. 1e**. Signals corresponding to phospho-ERM were
903 normalized to that for ERM. Statistical significance was determined by One-way ANOVA
904 [F (2, 9) = 354.8, p < 0.0001], Bonferroni multiple comparison revealed a significant
905 difference between 0 nM and 30 nM MLi-2 treatments (p < 0.0001, 95% C.I. = [0.6566,
906 0.8600]) and between 0 nM and 100 nM MLi-2 treatments (p < 0.0001, 95% C.I. = [0.7341,
907 0.9375]) and no differences between 30 nM and 100 nM MLi-2 treatments (p = 0.1568,
908 95% C.I. = [-0.02422, 0.1792]), alpha = 0.05. **g,** WT or LRRK2 G2019S astrocytes were
909 lysed and subjected to Western blotting, using phospho-ERM and ERM antibodies.
910 Results are representative of 3 independent experiments. **h,** Densitometric analysis of
911 phospho-ERM levels in **Fig. 1g**. Signals corresponding to phospho-ERM were normalized

912 to that for ERM. Statistical significance was determined by Unpaired Two-tailed t-test [t
913 (5.944) = 5.536], p = 0.0015. **i,** (Upper) Representative rat cortical astrocytes transfected
914 shControl-GFP + WT EZRIN, shControl-GFP + Phospho-mimetic EZRIN, and co-cultured
915 with WT cortical neurons. Scale bar, 10 μm. (Lower) Quantification of astrocyte branching
916 complexity. n = 47 (shControl-GFP + WT EZRIN O/E), 46 (shControl-GFP + Phospho-
917 mimetic EZRIN O/E) astrocytes co-cultured with WT cortical neurons compiled from three
918 independent experiments. We fitted a linear mixed model with number of intersections as
919 outcome variable, condition as predictor and number of cells and cell radius were entered
920 as random effects. Within this model, neither WT EZRIN (beta = 14.76, t(107) = 19.17) or
921 Phospho-mimetic EZRIN (beta = 13.22, t(107) = 19.07) lead to significant changes of
922 number of intersections of shControl-GFP astrocytes (beta = 12.75, t(107) = 19.82).
923 Tukey multiple comparisons test revealed no difference between shControl-GFP and
924 shControl-GFP + WT EZRIN O/E (p = 0.1110), shControl-GFP and shControl-GFP +
925 Phospho-mimetic EZRIN O/E (p = 0.8727), and shControl-GFP + WT EZRIN O/E and
926 shControl-GFP + Phospho-mimetic EZRIN O/E (p = 0.2969). **j,** (Upper) Representative
927 rat cortical astrocytes transfected sh*Lrrk2*-GFP + WT EZRIN, sh*Lrrk2*-GFP + Phospho-
928 mimetic EZRIN, and co-cultured with WT cortical neurons. Scale bar, 10 μm. (Lower)
929 Quantification of astrocyte branching complexity. n = 55 (sh*Lrrk2*-GFP + WT EZRIN O/E),
930 47 (sh*Lrrk2*-GFP + Phospho-mimetic EZRIN O/E) astrocytes co-cultured with WT cortical
931 neurons compiled from three independent experiments. We fitted a linear mixed model
932 with number of intersections as outcome variable, condition as predictor and number of
933 cells and cell radius were entered as random effects. Within this model, WT EZRIN (beta
934 = 4.99, t(162) = 10.32) did not increase the number of intersections of sh*Lrrk2*-GFP

935 astrocytes but Phospho-mimetic EZRIN (beta = 15.27, t(162) = 27.93) increased number
936 of intersections of shLRRK2-GFP astrocytes (beta = 4.80, t(162) = 10.63). Tukey multiple
937 comparisons test revealed no difference between sh*Lrrk2*-GFP and sh*Lrrk2*-GFP + WT
938 EZRIN O/E (p = 0.9926). Tukey multiple comparisons test revealed significant difference
939 between sh*Lrrk2*-GFP and sh*Lrrk2*-GFP + Phospho-mimetic EZRIN O/E (p < 0.0001). **k-**
940 **l,** (Upper) Representative WT **(k)** or LRRK2 G2019S **(l)** rat astrocytes transfected GFP +
941 WT EZRIN, or GFP + Phospho-dead EZRIN, and co-cultured with WT cortical neurons,
942 respectively. Scale bar, 10 µm. (Lower) Quantification of astrocyte branching complexity.
943 n = 57 (WT + WT EZRIN O/E), 66 (WT + Phospho-dead EZRIN O/E), 57 (LRRK2 G2019S
944 + WT EZRIN O/E), 48 (LRRK2 G2019S + Phospho-dead EZRIN O/E) astrocytes co-
945 cultured with WT cortical neurons compiled from three independent experiments. We
946 fitted a linear mixed model with number of intersections as outcome variable, condition
947 as predictor and number of cells and cell radius were entered as random effects. Within
948 this model, WT EZRIN (beta = 13.49, t(137) = 25.15) did not change the number of
949 intersections of WT astrocytes, but Phospho-dead EZRIN (beta = 5.37, t(137) = 10.02)
950 decreased number of intersections of WT astrocytes (beta = 10.86, t(137) = 24.82). WT
951 EZRIN (beta = 7.52, t(209) = 15.91) did not change the number of intersections of LRRK2
952 G2019S astrocytes but Phospho-dead EZRIN (beta = 10.88, t(209) = 22.54) increased
953 number of intersections of LRRK2 G2019S astrocytes (beta = 7.55, t(209) = 16.77). Tukey
954 multiple comparisons test revealed a significant difference between LRRK2 G2019S and
955 LRRK2 G2019S + Phospho-mimetic EZRIN O/E (p = 2.03E-06), and LRRK2 G2019S +
956 WT EZRIN O/E and LRRK2 G2019S + Phospho-mimetic EZRIN O/E (p = 4.83E-06).
957 Tukey multiple comparisons test revealed no difference between LRRK2 G2019S and

958 LRRK2 G2019S + WT EZRIN O/E (p = 0.9999), and between WT and LRRK2 G2019S +
959 Phospho-mimetic EZRIN O/E (p = 0.9999). Data are presented as mean ± s.e.m.

960 **Extended Data Figure 1 (related to Figure 1). Localization and expression of LRRK2**
961 **in astrocytes. a-b,** LRRK2 (red) in the primary motor cortex (MOp) of LRRK2 G2019S$^{ki/ki}$;
962 Aldh1l1-eGFP mice at P21. Scale bar, 10 μm. **c,** Cultured WT and LRRK2 KO rat cortical
963 astrocytes were lysed, and cytoplasmic proteins were subjected to Western blotting, using
964 LRRK2 and β-actin antibodies. Results are representative of 4 independent experiments.
965 **d,** Densitometric analysis of LRRK2 levels in **Extended Data Fig. 1c**. Signals
966 corresponding to LRRK2 were normalized to that for β-actin. Relative LRRK2 levels were
967 then normalized to the LRRK2 signals in WT rat cortical astrocytes. Statistical significance
968 was determined by an Unpaired Two-tailed t-test [t (6) = 13.79], $p < 0.0001$. **e,** Cultured
969 WT and LRRK2 G2019S rat cortical astrocytes were lysed, and cytoplasmic proteins were
970 subjected to Western blotting using LRRK2 and β-actin antibodies. Results are
971 representative of 3 independent experiments. **f,** Densitometric analysis of LRRK2 levels
972 in **Extended Data Fig. 1e**. Signals corresponding to LRRK2 were normalized to that for
973 β-actin. Relative LRRK2 levels were then normalized to the LRRK2 signals in WT rat
974 cortical astrocytes. Statistical significance was determined by an Unpaired Two-tailed t-
975 test [t (4) = 47.96], $p < 0.0001$. **g,** Cultured WT, and shControl and sh*Lrrk2* transfected
976 rat cortical astrocytes were lysed, and cytoplasmic proteins were subjected to Western
977 blotting using LRRK2 and GAPDH antibodies. Results are representative of 3
978 independent experiments. **h,** Densitometric analysis of LRRK2 levels in **Extended Data**
979 **Fig. 1g**. Signals corresponding to LRRK2 were first normalized to that for β-actin. Relative
980 LRRK2 levels were then normalized to the LRRK2 signals in WT rat cortical astrocytes.

981 Statistical significance was determined by One-way ANOVA [F (2, 6) = 92.25, $p < 0.0001$],
982 Bonferroni multiple comparison revealed a significant difference between WT and sh*Lrrk2*
983 ($p < 0.0001$, 95% C.I. = [0.6743, 1.183]) and between sh*Lrrk2* and shControl ($p < 0.0001$,
984 95% C.I. = [-1.145, -0.6363]) and no differences between WT and shControl ($p > 0.9999$,
985 95% C.I. = [-0.2165, 0.2923]), alpha = 0.05. **i-j,** Bar plots of Ezr, Rdx, and Msn gene
986 expression in various brain cell types in mice (yellow) or humans (red). These plots are
987 generated using publicly available data at https://www.brainrnaseq.org/[52,172].

988 **Figure 2. Astrocytic LRRK2 controls astrocyte morphology by balancing ERM**
989 **phosphorylation levels *in vivo*. a-c,** Representative confocal images of ERM
990 phosphorylation (purple) in the anterior cingulate cortex (ACC) and primary motor cortex
991 (MOp) of WT or LRRK2 G2019S$^{ki/ki}$ Aldh1l1-eGFP transgenic mice at P21. Scale bar, 200
992 µm (**a-b**). Scale bar, 10 µm (**c**). **d,** Quantification of phospho-ERM integrated density in
993 **a-b**, n = 4 (WT, 2 males and 2 females), 4 (LRRK2 G2019S$^{ki/ki}$, 2 males and 2 females)
994 mice, For phospho-ERM quantification in the ACC, nested t-test, unpaired Two-tailed t-
995 test. t (16) = 15.16, $p < 0.0001$. For phospho-ERM quantification in the MOp, nested t-
996 test, unpaired Two-tailed t-test. t (14) = 8.963, $p < 0.0001$. Grey dots are the data acquired
997 from each image. Black dots are the averaged data acquired from each WT mouse. Blue
998 dots are the averaged data acquired from each LRRK2 G2019S$^{ki/ki}$ mouse. **e,** Images of
999 ACC and MOp layer 2/3 WT and LRRK2 G2019S$^{ki/ki}$ astrocytes at P21 expressing PB-
1000 mCherry-CAAX ± Phospho-dead EZRIN. Astrocyte territory in cyan. Scale bar, 10 µm. **f,**
1001 Average territory volumes of P21 astrocytes. n = 16 (WT; 6 mice), 18 (WT + Phospho-
1002 dead EZRIN O/E; 6 mice), 16 (LRRK2 G2019S; 6 mice), 17 (LRRK2 G2019S + Phospho-
1003 dead EZRIN O/E; 6 mice). Statistical significance was determined by One-way ANOVA

1004 [F (3, 20) = 7.987, p = 0.0011], Bonferroni multiple comparisons revealed a significant
1005 difference between WT and LRRK2 G2019S (p = 0.0178, 95% C.I. = [0.4542, 6.313]),
1006 between WT and WT + Phospho-dead EZRIN O/E (p = 0.0037, 95% C.I. = [1.132, 6.991]),
1007 and between WT + Phospho-dead EZRIN O/E and LRRK2 G2019S + Phospho-mimetic
1008 EZRIN O/E (p = 0.0165, 95% C.I. = [-6.346, -0.4875]), and no differences between WT
1009 and LRRK2 G2019S + Phospho-mimetic EZRIN O/E (p > 0.9999, 95% C.I. = [-2.284,
1010 3.574]), between LRRK2 G2019S and WT + Phospho-dead EZRIN O/E (p > 0.9999, 95%
1011 C.I. = [-2.251, 3.608]), and between LRRK2 G2019S and LRRK2 G2019S + Phospho-
1012 mimetic EZRIN O/E (p = 0.0763, 95% C.I. = [-5.668, 0.1908]), alpha = 0.05. Data points
1013 are mouse averages. **g,** Quantification of astrocyte branching complexity. n = 16 (WT; 6
1014 mice), 18 (WT + Phospho-dead EZRIN O/E; 6 mice), 16 (LRRK2 G2019S; 6 mice), 17
1015 (LRRK2 G2019S + Phospho-dead EZRIN O/E; 6 mice). Two-way ANOVA for repeated
1016 measures. Main effects of conditions [F (2.505, 3305) = 158.4, p < 0.0001] and radius [F
1017 (88, 1602) = 218.5, p < 0.0001] and interaction [F (264, 3958) = 10.62, p < 0.0001].
1018 Bonferroni multiple comparisons revealed a significant difference between WT and
1019 LRRK2 G2019S (p < 0.0001, 95% C.I. = [16.09, 26.40]), between WT and WT + Phospho-
1020 dead EZRIN O/E (p < 0.0001, 95% C.I. = [29.06, 39.54]), between LRRK2 G2019S and
1021 WT + Phospho-dead EZRIN O/E (p < 0.0001, 95% C.I. = [7.6, 18.52]), between LRRK2
1022 G2019S and LRRK2 G2019S + Phospho-dead EZRIN O/E (p < 0.0001, 95% C.I. = [-
1023 22.19, -13.43]), and between WT + Phospho-dead EZRIN O/E and LRRK2 G2019S +
1024 Phospho-dead EZRIN O/E (p < 0.0001, 95% C.I. = [-37.02, -24.72]), and no difference
1025 between WT and LRRK2 G2019S + Phospho-dead EZRIN O/E (p = 0.5469, 95% C.I. =
1026 [-1.932, 8.796]). **h,** Images of ACC and MOp layer 2/3 astrocytes at P21 expressing

1027 shControl-mCherry-CAAX or sh*Lrrk2*-mCherry-CAAX ± Phospho-mimetic EZRIN.
1028 Astrocyte territory in cyan. Scale bar, 10 µm. **i,** Average territory volumes of P21
1029 astrocytes. n = 18 (shControl; 6 mice), 18 (shControl + Phospho-mimetic EZRIN O/E; 5
1030 mice), 22 (sh*Lrrk2*; 6 mice), 19 (sh*Lrrk2* + Phospho-mimetic EZRIN O/E; 7 mice).
1031 Statistical significance was determined by One-way ANOVA [F (3, 20) = 5.674, p =
1032 0.0056], Bonferroni multiple comparison revealed a significant difference between
1033 shControl and sh*Lrrk2* (p = 0.0104, 95% C.I. = [0.5585, 5.322]), and between sh*Lrrk2* and
1034 sh*Lrrk2* + Phospho-mimetic EZRIN O/E (p = 0.0114, 95% C.I. = [-5.096, -0.5065]), and
1035 no differences between shControl and shControl + Phospho-mimetic EZRIN O/E (p >
1036 0.9999, 95% C.I. = [-1.426, 3.570]), between shControl and sh*Lrrk2* + Phospho-mimetic
1037 EZRIN O/E (p > 0.9999, 95% C.I. = [-2.156, 2.433]), and between shControl + Phospho-
1038 mimetic EZRIN O/E and sh*Lrrk2* + Phospho-mimetic EZRIN O/E (p > 0.9999, 95% C.I. =
1039 [-3.349, 1.482]), alpha = 0.05. Data points are mouse averages. **j,** Quantification of
1040 astrocyte branching complexity. n = 16 (shControl), 24 (shControl + Phospho-mimetic
1041 EZRIN O/E), 23 (sh*Lrrk2*), 18 (sh*Lrrk2* + Phospho-mimetic EZRIN O/E). Two-way ANOVA
1042 for repeated measures. Main effects of conditions [F (2.435, 7008) = 225.0, p < 0.0001]
1043 and radius [F (88, 8633) = 325.4, p < 0.0001] and interaction [F (264, 8633) = 5.908, p <
1044 0.0001]. Bonferroni multiple comparisons revealed a significant difference between
1045 shControl and sh*Lrrk2* (p < 0.0001, 95% C.I. = [31.02, 40.20]), between sh*Lrrk2* and
1046 shControl + Phospho-mimetic EZRIN O/E (p < 0.0001, 95% C.I. = [-38.59, -29.67]),
1047 between sh*Lrrk2* and sh*Lrrk2* + Phospho-mimetic EZRIN O/E (p < 0.0001, 95% C.I. = [-
1048 34.32, -25.69]), between shControl and sh*Lrrk2* + Phospho-mimetic EZRIN O/E (p =
1049 0.0139, 95% C.I. = [0.7510, 10.47]), and between shControl + Phospho-mimetic EZRIN

1050 O/E and sh*Lrrk2* + Phospho-mimetic EZRIN O/E (p = 0.0188, 95% C.I. = [0.4426, 7.813]),
1051 and no difference between shControl and shControl + Phospho-mimetic EZRIN O/E (p >
1052 0.9999, 95% C.I. = [-3.083, 6.044]). Data are presented as mean ± s.e.m. **k,** Schematic
1053 representation of analyzed human brain regions for phospho-ERM staining, frontal cortex.
1054 **l,** Representative confocal images of GFAP (green) and ERM phosphorylation (purple) in
1055 the frontal cortex of human control subjects or human PD patients carrying LRRK2
1056 G2019S mutation carriers at age >80 years old. Scale bar, 200 μm. n = 4 (Human control,
1057 3 males and 1 female), 3 (LRRK2 G2019S mutation carriers, 2 males and 1 female)
1058 subjects. **m,** Quantification of phospho-ERM integrated density in **l**, n = 4 (Human control,
1059 3 males and 1 female), 3 (LRRK2 G2019S mutation carriers, 2 males and 1 female)
1060 subjects, nested t-test, unpaired Two-tailed t-test. t (4) = 3.551, p = 0.0238. The grey dot
1061 is the data acquired from each image. The black dot is the averaged data acquired from
1062 each control subject. The blue dot is the averaged data acquired from each LRRK2
1063 G2019S mutation carrier. **n,** Quantification of GFAP integrated density in **l**, n = 4 (Human
1064 control, 3 males and 1 female), 3 (LRRK2 G2019S mutation carriers, 2 males and 1
1065 female) subjects, nested t-test, unpaired Two-tailed t-test. t (18) = 3.612, p = 0.0020. Grey
1066 dots are the data acquired from each image. Black dots are the averaged data acquired
1067 from each control subject. Blue dots are the averaged data acquired from each LRRK2
1068 G2019S mutation carrier.

1069 **Extended Data Figure 2 (related to Figure 2). Phospho-ERM is upregulated in**
1070 **LRRK2 G2019S$^{ki/ki}$ astrocytes in ACC and MOp but not SSp and DMS. a-b,**
1071 Representative confocal images of ERM phosphorylation (purple) in the MOp and ACC
1072 of WT or LRRK2 G2019S$^{ki/ki}$ Aldh1l1-eGFP transgenic mice at P84. Scale bar, 200 μm. n

1073 = 4 (WT, 2 males and 2 females), 4 (LRRK2 G2019S$^{ki/ki}$, 2 males and 2 females) mice. **c,**
1074 Quantification of phospho-ERM integrated density in **a-b**, n = 4 (WT, 2 males and 2
1075 females), 4 (LRRK2 G2019S$^{ki/ki}$, 2 males and 2 females) mice, For phospho-ERM
1076 quantification in the ACC, nested t-test, unpaired Two-tailed t-test. t (14) = 11.84, p <
1077 0.0001. For phospho-ERM quantification in the MOp, nested t-test, unpaired Two-tailed
1078 t-test. t (14) = 6.585, p < 0.0001. Grey dots are the data acquired from each image. Black
1079 dots are the averaged data acquired from each WT mouse. Blue dots are the averaged
1080 data acquired from each LRRK2 G2019S$^{ki/ki}$ mouse. **d-e,** Representative confocal images
1081 of ERM phosphorylation (purple) in the MOp and ACC of WT or LRRK2 G2019S$^{ki/ki}$
1082 Aldh1l1-eGFP transgenic mice at P84. Scale bar, 20 μm. **f-g,** Representative confocal
1083 images of ERM phosphorylation (purple) in the SSp and DMS of WT or LRRK2 G2019S$^{ki/ki}$
1084 Aldh1l1-eGFP transgenic mice at P21. Scale bar, 200 μm. n = 4 (WT, 2 males and 2
1085 females), 4 (LRRK2 G2019S$^{ki/ki}$, 2 males and 2 females) mice. **h,** Quantification of
1086 phospho-ERM integrated density in **f-g** and **i-j**, n = 4 (WT, 2 males and 2 females), 4
1087 (LRRK2 G2019S$^{ki/ki}$, 2 males and 2 females) mice. For phospho-ERM integrated density
1088 at P21, nested t-test, unpaired Two-tailed t-test. t (22) = 0.1556, p = 0.8777. For phospho-
1089 ERM integrated density at 12-week-old, nested t-test, unpaired Two-tailed t-test. t (4) =
1090 0.5028, p = 0.6415. Grey dots are the data acquired from each image. Black dots are the
1091 averaged data acquired from each WT mouse. Blue dots are the averaged data acquired
1092 from each LRRK2 G2019S$^{ki/ki}$ mouse. **i-j,** Representative confocal images of ERM
1093 phosphorylation (purple) in the SSp and DMS of WT or LRRK2 G2019S$^{ki/ki}$ Aldh11-eGFP
1094 transgenic mice at P84. Scale bar, 200 μm. n = 4 (WT, 2 males and 2 females), 4 (LRRK2

1095 G2019S$^{ki/ki}$, 2 males and 2 females) mice. **k,** Overview of postnatal astrocyte labeling by
1096 electroporation (PALE) with PiggyBac plasmids.

1097 **Extended Data Figure 3 (related to Figure 2). LRRK2 G2019S does not change GFAP**
1098 **level and ALDH1L1+/SOX9+ cell numbers in the ACC and MOp. a-b,** Representative
1099 confocal images of SOX9 (purple) in the ACC and MOp of WT or LRRK2 G2019S$^{ki/ki}$
1100 Aldh1l1-eGFP transgenic mice at P21. Scale bar, 200 μm. **c,** Quantification of
1101 ALDH1L1+/SOX9+ cell numbers in **a-b**, n = 3 (WT, 2 males and 1 female), 3 (LRRK2
1102 G2019S$^{ki/ki}$, 2 males and 1 female) mice, For ALDH1L1+/SOX9+ cell counting in the ACC,
1103 nested t-test, unpaired Two-tailed t-test. t (9) = 1.533, p = 0.2470. For ALDH1L1+/SOX9+
1104 cell counting in the MOp, nested t-test, unpaired Two-tailed t-test. t (2) = 1.544, p = 0.2625.
1105 Grey dots are the data acquired from each image. Black dots are the averaged data
1106 acquired from each WT mouse. Blue dots are the averaged data acquired from each
1107 LRRK2 G2019S$^{ki/ki}$ mouse. **d-e,** Representative confocal images of GFAP (purple) in the
1108 ACC and MOp of WT or LRRK2 G2019S$^{ki/ki}$ Aldh1l1-eGFP transgenic mice at P21. Scale
1109 bar, 200 μm. **f,** Quantification of GFAP integrated density in **d-e**, n = 3 (WT, 2 males and
1110 1 female), 3 (LRRK2 G2019S$^{ki/ki}$, 2 males and 1 female) mice, For GFAP quantification in
1111 the ACC, nested t-test, unpaired Two-tailed t-test. t (10) = 1.524, p = 0.1586. For GFAP
1112 quantification in the MOp, nested t-test, unpaired Two-tailed t-test. t (10) = 0.5028, p =
1113 0.6260. Grey dots are the data acquired from each image. Black dots are the averaged
1114 data acquired from each WT mouse. Blue dots are the averaged data acquired from each
1115 LRRK2 G2019S$^{ki/ki}$ mouse.

1116 **Figure 3. LRRK2 G2019S affects excitatory and inhibitory synapse number and**
1117 **function in the ACC and MOp. a,** Schematic representation of analyzed brain regions

1118 (ACC and MOp) for excitatory and inhibitory synapse numbers. **b,** Schematic
1119 representations of methodologies used to quantify the VGluT1-PSD95 and VGAT-
1120 GEPHYRIN colocalized puncta. **c,** (Left) Representative images from the ventral ACC
1121 layer 1 of WT and LRRK2 G2019S$^{ki/ki}$ mice that were stained with VGluT1 and PSD95
1122 antibodies at 12-week-old. Scale bar, 10 μm. (Right) Quantification of VGluT1/PSD95 co-
1123 localized puncta, normalized using the means of WT values in the ventral ACC layer 1. n
1124 = 5 (WT, 3 males and 2 females), 5 (LRRK2 G2019S$^{ki/ki}$, 3 males and 2 females) mice,
1125 nested t-test, unpaired Two-tailed t-test. t (28) = 4.358, p = 0.0002. **d,** (Left)
1126 Representative images from the ventral ACC layer 2/3 of WT and LRRK2 G2019S$^{ki/ki}$ mice
1127 that were stained with VGluT1 and PSD95 antibodies at 12-week-old. Scale bar, 10 μm.
1128 (Right) Quantification of VGluT1/PSD95 co-localized puncta, normalized using the means
1129 of WT values in the ventral ACC layer 2/3. n = 5 (WT, 3 males and 2 females), 5 (LRRK2
1130 G2019S$^{ki/ki}$, 3 males and 2 females) mice, nested t-test, unpaired Two-tailed t-test. t (28)
1131 = 4.287, p = 0.0002. **e**, (Left) Representative images from MOp layer 1 of WT and LRRK2
1132 G2019S$^{ki/ki}$ mice that were stained with VGAT and GEPHYRIN antibodies at 12-week-old.
1133 Scale bar, 10 μm. (Right) Quantification of VGAT/GEPHYRIN co-localized puncta,
1134 normalized using the means of WT values in MOp layer 1. n = 6 (WT, 3 males and 3
1135 females), 6 (LRRK2 G2019S$^{ki/ki}$, 3 males and 3 females) mice, nested t-test, unpaired
1136 Two-tailed t-test. t (34) = 7.164, p < 0.0001. **f**, (Left) Representative images from MOp
1137 layer 2/3 of WT and LRRK2 G2019S$^{ki/ki}$ mice that were stained with VGAT and
1138 GEPHYRIN antibodies at 12-week-old. Scale bar, 10 μm. (Right) Quantification of
1139 VGAT/GEPHYRIN co-localized puncta, normalized using the means of WT values in MOp
1140 layer 2/3. n = 6 (WT, 3 males and 3 females), 6 (LRRK2 G2019S$^{ki/ki}$, 3 males and 3

1141 females) mice, nested t-test, unpaired Two-tailed t-test. t (34) = 5.25, $p < 0.0001$. **g,**
1142 Representative mEPSC traces from the ventral ACC layer 2/3 pyramidal neurons in acute
1143 brain slices of WT and LRRK2 G2019S$^{ki/ki}$ mice. **h,** Cumulative frequency plots and
1144 quantification of synaptic event frequency, n = 15 (WT), 13 (LRRK2 G2019S$^{ki/ki}$) neurons
1145 from 4 mice per genotype. Kolmogorov-Smirnov test (D = 0.504, $p < 0.001$). The average
1146 frequency of mEPSC in WT (2.521 ± 0.3846) and LRRK2 G2019S$^{ki/ki}$ (0.8691 ± 0.1309)
1147 mice. Unpaired Two-tailed t-test [t (26) = 3.828, $p = 0.0007$]. **i,** Cumulative frequency plots
1148 and quantification of synaptic event amplitude, n = 15 (WT), 13 (LRRK2 G2019S$^{ki/ki}$)
1149 neurons from 4 mice per genotype. Kolmogorov-Smirnov test (D = 0.194, $p < 0.0001$).
1150 The average amplitude of mEPSC in WT (15.53 ± 0.8105) and LRRK2 G2019S$^{ki/ki}$ (13.52
1151 ± 0.5818) mice. Unpaired t-test [t (26) = 1.951, $p = 0.0619$]. **j**, Representative mIPSC
1152 traces from MOp layer 2/3 pyramidal neurons in acute brain slices of WT and LRRK2
1153 G2019S$^{ki/ki}$ mice. **k**, Cumulative frequency plots and quantification of synaptic event
1154 frequency, n = 12 (WT), 11 (LRRK2 G2019S$^{ki/ki}$) neurons from 4 mice per genotype.
1155 Kolmogorov-Smirnov test (D = 0.424, $p < 0.0001$). The average frequency of mIPSC in
1156 WT (0.7606 ± 0.06816) and LRRK2 G2019S$^{ki/ki}$ (1.312 ± 0.1041) mice. Unpaired Two-
1157 tailed t-test [t (21) = 4.503, $p = 0.0002$]. **l**, Cumulative frequency plots and quantification
1158 of synaptic event amplitude, n = 12 (WT), 11 (LRRK2 G2019S$^{ki/ki}$) neurons from 4 mice
1159 per genotype. Kolmogorov-Smirnov test (D = 0.382, $p < 0.0001$). The average amplitude
1160 of mIPSC in WT (8.776 ± 0.4961) and LRRK2 G2019S$^{ki/ki}$ (9.921 ± 0.5043) mice. Unpaired
1161 t-test [t (21) = 1.617, $p = 0.1209$]. Data are presented as mean ± s.e.m.

1162 **Extended Data Figure 4 (related to Figure 3). LRRK2 G2019S does not change**
1163 **excitatory synapse numbers in the primary motor cortex. a,** (Left) Representative

1164 images from the ventral ACC layer 1 of WT and LRRK2 G2019S$^{ki/ki}$ mice that were stained
1165 with VGAT and GEPHYRIN antibodies at 12-week-old. Scale bar, 10 μm. (Right)
1166 Quantification of VGAT/GEPHYRIN co-localized puncta, normalized using the means of
1167 WT values in the ventral ACC layer 1. n = 4 (WT, 2 males and 2 females), 4 (LRRK2
1168 G2019S$^{ki/ki}$, 2 males and 2 females) mice, nested t-test, unpaired Two-tailed t-test. t (22)
1169 = 0.3365, p = 0.7397. Grey dots are the data acquired from each synapse image. Black
1170 dots are the averaged data acquired from each WT mouse. Blue dots are the averaged
1171 data acquired from each LRRK2 G2019S$^{ki/ki}$ mouse. **b,** (Left) Representative images from
1172 the ventral ACC layer 2/3 of WT and LRRK2 G2019S$^{ki/ki}$ mice that were stained with VGAT
1173 and GEPHYRIN antibodies at 12-week-old. Scale bar, 10 μm. (Right) Quantification of
1174 VGAT/GEPHYRIN co-localized puncta, normalized using the means of WT values in the
1175 ventral ACC layer 2/3. n = 4 (WT, 2 males and 2 females), 4 (LRRK2 G2019S$^{ki/ki}$, 2 males
1176 and 2 females) mice, nested t-test, unpaired Two-tailed t-test. t (21) = 0.4692, p = 0.6438.
1177 **c,** (Left) Representative images from the MOp layer 1 of WT and LRRK2 G2019S$^{ki/ki}$ mice
1178 that were stained with VGluT1 and PSD95 antibodies at 12-week-old. Scale bar, 10 μm.
1179 (Right) Quantification of VGluT1/PSD95 co-localized puncta in **c**, normalized using the
1180 means of WT values in the MOp layer 1. n = 5 (WT), 5 (LRRK2 G2019S$^{ki/ki}$) mice, 3 males
1181 and 2 females, nested t-test, unpaired Two-tailed t-test. t (28) = 1.012, p = 0.3203. **d,**
1182 (Left) Representative images from the MOp layer 2/3 of WT and LRRK2 G2019S$^{ki/ki}$ mice
1183 that were stained with VGluT1 and PSD95 antibodies at 12-week-old. Scale bar, 10 μm.
1184 (Right) Quantification of VGluT1/PSD95 co-localized puncta in **c**, normalized using the
1185 means of WT values in the MOp layer 2/3. n = 5 (WT), 5 (LRRK2 G2019S$^{ki/ki}$) mice, 3
1186 males and 2 females, nested t-test, unpaired Two-tailed t-test. t (4) = 0.20465, p = 0.8479.

1187 **Figure 4. Overexpression of phospho-dead EZRIN in adult LRRK2 G2019S$^{ki/ki}$**
1188 **astrocytes restores excitatory synapse number and function in the ventral ACC. a,**
1189 Representative images from the ventral ACC layer 1 of WT and LRRK2 G2019S$^{ki/ki}$ mice
1190 injected with AAV-HA-tagged-WT EZRIN or AAV-HA-tagged-Phospho-dead EZRIN that
1191 were stained with VGluT1 and PSD95 antibodies at 12-week-old. Scale bar, 10 μm.
1192 Quantification of VGluT1/PSD95 co-localized puncta, normalized using the means of WT
1193 mice injected with AAV-HA-tagged-WT EZRIN in the ventral ACC layer 1. n = 6 (WT +
1194 WT EZRIN O/E, 3 males and 3 females), 5 (WT + Phospho-dead Ezrin O/E, 3 males and
1195 2 females), 6 (LRRK2 G2019S$^{ki/ki}$ + WT EZRIN O/E, 3 males and 3 females), 6 (LRRK2
1196 G2019S$^{ki/ki}$ + Phospho-dead EZRIN O/E, 3 males and 3 females) mice. One-way ANOVA
1197 [F (3, 19) = 5.882, p = 0.0051], Bonferroni's multiple comparisons test revealed a
1198 significant difference between WT + WT EZRIN O/E and WT + Phospho-dead Ezrin O/E
1199 (p = 0.0493, 95% C.I. = [0.05586, 53.21]), between WT + WT EZRIN O/E and LRRK2
1200 G2019S$^{ki/ki}$ + WT EZRIN O/E (p = 0.0269, 95% C.I. = [2.396, 53.08]), and between LRRK2
1201 G2019S$^{ki/ki}$ + WT EZRIN O/E and LRRK2 G2019S$^{ki/ki}$ + Phospho-dead Ezrin O/E (p =
1202 0.049, 95% C.I. = [-50.77, -0.08163]). There were no differences between WT + WT
1203 EZRIN O/E and LRRK2 G2019S$^{ki/ki}$ + Phospho-dead Ezrin O/E (p > 0.9999, 95% C.I. = [-
1204 23.03, 27.66]), between WT + Phospho-dead Ezrin O/E and LRRK2 G2019S$^{ki/ki}$ + WT
1205 EZRIN O/E (p > 0.9999, 95% C.I. = [-25.48, 27.68]), and between WT + Phospho-dead
1206 Ezrin O/E and LRRK2 G2019S$^{ki/ki}$ + Phospho-dead Ezrin O/E (p = 0.0863, 95% C.I. = [-
1207 50.90, 2.259]), alpha = 0.05. **b,** Representative images from the ventral ACC layer 2/3 of
1208 WT and LRRK2 G2019S$^{ki/ki}$ mice injected with AAV-HA-tagged-WT EZRIN or AAV-HA-
1209 tagged-Phospho-dead EZRIN that were stained with VGluT1 and PSD95 antibodies at

1210 12-week-old. Scale bar, 10 μm. Quantification of VGluT1/PSD95 co-localized puncta,
1211 normalized using the means of WT mice injected with AAV-HA-tagged-WT EZRIN in the
1212 ventral ACC layer 2/3. n = 6 (WT + WT EZRIN O/E, 3 males and 3 females), 5 (WT +
1213 Phospho-dead EZRIN O/E, 3 males and 2 females), 6 (LRRK2 G2019S$^{ki/ki}$ + WT EZRIN
1214 O/E, 3 males and 3 females), 6 (LRRK2 G2019S$^{ki/ki}$ + Phospho-dead EZRIN O/E, 3 males
1215 and 3 females) mice. One-way ANOVA [F (3, 18) = 10.45, p = 0.0003], Bonferroni's
1216 multiple comparisons test revealed a significant difference between WT + WT EZRIN O/E
1217 and WT + Phospho-dead Ezrin O/E (p = 0.0041, 95% C.I. = [8.857, 55.39]), between WT
1218 + WT EZRIN O/E and LRRK2 G2019S$^{ki/ki}$ + WT EZRIN O/E (p = 0.0016, 95% C.I. = [11.67,
1219 56.22]), between WT + Phospho-dead EZRIN O/E and LRRK2 G2019S$^{ki/ki}$ + Phospho-
1220 dead EZRIN O/E (p = 0.0232, 95% C.I. = [-47.19.67, -2.636]) and between LRRK2
1221 G2019S$^{ki/ki}$ + WT EZRIN O/E and LRRK2 G2019S$^{ki/ki}$ + Phospho-dead Ezrin O/E (p =
1222 0.0092, 95% C.I. = [-47.97.77, -5.494]). There were no differences between WT + WT
1223 EZRIN O/E and LRRK2 G2019S$^{ki/ki}$ + Phospho-dead Ezrin O/E (p > 0.9999, 95% C.I. = [-
1224 15.06, 29.49]), and between WT + Phospho-dead Ezrin O/E and LRRK2 G2019S$^{ki/ki}$ +
1225 WT EZRIN O/E (p > 0.9999, 95% C.I. = [-20.45, 24.10]), alpha = 0.05. **c,** Representative
1226 mEPSC traces from the ventral ACC layer 2/3 pyramidal neurons in acute brain slices of
1227 WT and LRRK2 G2019S$^{ki/ki}$ mice injected with AAV-HA-tagged-WT EZRIN or AAV-HA-
1228 tagged-Phospho-dead EZRIN. **d,** Cumulative frequency plots and quantification of
1229 synaptic event frequency. n = 14 (WT + WT EZRIN O/E), 15 (WT + Phospho-dead EZRIN
1230 O/E), 11 (LRRK2 G2019S$^{ki/ki}$ + WT EZRIN O/E), 14 (LRRK2 G2019S$^{ki/ki}$ + Phospho-dead
1231 EZRIN O/E) neurons from 4 mice per condition. Kruskal-Wallis test [H (3) = 36.83, p <
1232 0.0001]. Average frequency of mEPSC in WT + WT EZRIN O/E (1.555 ± 0.1125), WT +

1233 Phospho-dead EZRIN O/E (0.8416 ± 0.05145), LRRK2 G2019S$^{ki/ki}$ + WT EZRIN O/E
1234 (0.7154 ± 0.05959), and LRRK2 G2019S$^{ki/ki}$ + Phospho-dead EZRIN O/E (1.253 ±
1235 0.04424) mice. The posthoc Dunn's test with Bonferroni adjustments showed to be
1236 significant for WT + WT EZRIN O/E vs. WT + Phospho-dead EZRIN O/E (p < 0.0001),
1237 WT + WT EZRIN O/E vs. LRRK2 G2019S$^{ki/ki}$ + WT EZRIN O/E (p < 0.0001), WT +
1238 Phospho-dead EZRIN O/E vs. LRRK2 G2019S$^{ki/ki}$ + Phospho-dead EZRIN O/E (p =
1239 0.0084), and LRRK2 G2019S$^{ki/ki}$ + WT EZRIN O/E vs. LRRK2 G2019S$^{ki/ki}$ + Phospho-
1240 dead EZRIN O/E (p = 0.0005). The posthoc Dunn's test with Bonferroni adjustments
1241 revealed no significant difference between WT + WT EZRIN O/E and LRRK2 G2019S$^{ki/ki}$
1242 + Phospho-dead EZRIN O/E (p > 0.9999) and between WT + Phospho-dead EZRIN O/E
1243 and LRRK2 G2019S$^{ki/ki}$ + WT EZRIN O/E (p > 0.9999). **e,** Cumulative frequency plots and
1244 quantification of synaptic event amplitude. n = 11 (WT + WT EZRIN O/E), 15 (WT +
1245 Phospho-dead EZRIN O/E), 11 (LRRK2 G2019S$^{ki/ki}$ + WT EZRIN O/E), 13 (LRRK2
1246 G2019S$^{ki/ki}$ + Phospho-dead EZRIN O/E) neurons from 4 mice per condition. Kruskal-
1247 Wallis test [H (3) = 7.051, p = 0.0703]. Average amplitude of mEPSC in WT + WT EZRIN
1248 O/E (4.873 ± 0.1034), WT + Phospho-dead EZRIN O/E (6.339 ± 0.4284), LRRK2
1249 G2019S$^{ki/ki}$ + WT EZRIN O/E (5.354 ± 0.2988), and LRRK2 G2019S$^{ki/ki}$ + Phospho-dead
1250 EZRIN O/E (5.591 ± 0.2247) mice. The posthoc Dunn's test with Bonferroni adjustments
1251 revealed no significant difference for WT + WT EZRIN O/E vs. WT + Phospho-dead
1252 EZRIN O/E (p = 0.0688), WT + WT EZRIN O/E vs. LRRK2 G2019S$^{ki/ki}$ + WT EZRIN O/E
1253 (p > 0.9999), WT + Phospho-dead EZRIN O/E vs. LRRK2 G2019S$^{ki/ki}$ + Phospho-dead
1254 EZRIN O/E (p > 0.9999), and LRRK2 G2019S$^{ki/ki}$ + WT EZRIN O/E vs. LRRK2 G2019S$^{ki/ki}$
1255 + Phospho-dead EZRIN O/E (p > 0.9999), WT + WT EZRIN O/E vs. LRRK2 G2019S$^{ki/ki}$

1256 + Phospho-dead EZRIN O/E (p = 0.3605), and WT + Phospho-dead EZRIN O/E vs.
1257 LRRK2 G2019S$^{ki/ki}$ + WT EZRIN O/E (p = 0.9468). alpha = 0.05. Data are presented as
1258 mean ± s.e.m.

1259 **Extended Data Figure 4 (related to Figure 5). Overexpression of AAV-HA-tagged-**
1260 **WT EZRIN and AAV-HA-tagged-Phospho-dead EZRIN in WT and LRRK2**
1261 **G2019S$^{ki/ki}$ astrocytes. a,** Experiment workflow of AAV-HA-tagged-WT EZRIN and
1262 AAV-HA-tagged-Phospho-dead EZRIN in WT and LRRK2 G2019S$^{ki/ki}$ astrocytes. **b,**
1263 Representative images from the ventral ACC of WT and LRRK2 G2019S$^{ki/ki}$ mice injected
1264 with AAV-HA-tagged-WT EZRIN or AAV-HA-tagged-Phospho-dead EZRIN that were
1265 stained with HA and phospho-ERM antibodies at 12-week-old. Scale bar, 200 μm. n = 6
1266 (WT + WT EZRIN O/E, 3 males and 3 females), 5 (WT + Phospho-dead EZRIN O/E, 3
1267 males and 2 females), 6 (LRRK2 G2019S$^{ki/ki}$ + WT EZRIN O/E, 3 males and 3 females),
1268 6 (LRRK2 G2019S$^{ki/ki}$ + Phospho-dead EZRIN O/E, 3 males and 3 females) mice. **c,**
1269 Representative images from the MOp layer 1 of WT and LRRK2 G2019S$^{ki/ki}$ mice injected
1270 with AAV-HA-tagged-WT EZRIN or AAV-HA-tagged-Phospho-dead EZRIN that were
1271 stained with VGAT and GEPHYRIN antibodies at 12-week-old. Scale bar, 10 μm.
1272 Quantification of VGAT/ GEPHYRIN co-localized puncta, normalized using the means of
1273 WT mice injected with AAV-HA-tagged-WT EZRIN in MOp layer 1. n = 3 (WT + WT EZRIN
1274 O/E, 2 males and 1 female), 5 (WT + Phospho-dead EZRIN O/E, 3 males and 2 females),
1275 6 (LRRK2 G2019S$^{ki/ki}$ + WT EZRIN O/E, 3 males and 3 females), 6 (LRRK2 G2019S$^{ki/ki}$
1276 + Phospho-dead EZRIN O/E, 3 males and 3 females) mice. One-way ANOVA [F (3, 55)
1277 = 19.7, p < 0.0001], Bonferroni's multiple comparisons test revealed a significant
1278 difference between WT + WT EZRIN O/E and LRRK2 G2019S$^{ki/ki}$ + WT EZRIN O/E (p <

1279 0.0001, 95% C.I. = [-98.23, -32.48]), and between WT + Phospho-dead EZRIN O/E and
1280 LRRK2 G2019S$^{ki/ki}$ + Phospho-dead EZRIN O/E (p < 0.0001, 95% C.I. = [-82.37, -26.61]).
1281 There were no differences between WT + WT EZRIN O/E and WT + Phospho-dead
1282 EZRIN O/E (p = 0.6323, 95% C.I. = [-53.85, 13.40]), and between LRRK2 G2019S$^{ki/ki}$ +
1283 WT EZRIN O/E and LRRK2 G2019S$^{ki/ki}$ + Phospho-dead EZRIN O/E (p > 0.9999, 95%
1284 C.I. = [-36.33, 17.61]), alpha = 0.05. **d,** Representative images from the MOp layer 2/3 of
1285 WT and LRRK2 G2019S$^{ki/ki}$ mice injected with AAV-HA-tagged-WT EZRIN or AAV-HA-
1286 tagged-Phospho-dead EZRIN that were stained with VGAT1 and GEPHYRIN antibodies
1287 at 12-week-old. Scale bar, 10 μm. Quantification of VGAT/GEPHYRIN co-localized
1288 puncta, normalized using the means of WT mice injected with AAV-HA-tagged-WT EZRIN
1289 in MOp layer 2/3. n = 3 (WT + WT EZRIN O/E, 2 males and 1 female), 5 (WT + Phospho-
1290 dead EZRIN O/E, 3 males and 2 females), 6 (LRRK2 G2019S$^{ki/ki}$ + WT EZRIN O/E, 3
1291 males and 3 females), 6 (LRRK2 G2019S$^{ki/ki}$ + Phospho-dead EZRIN O/E, 3 males and
1292 3 females) mice. One-way ANOVA [F (3, 54) = 15.10, p < 0.0001], Bonferroni's multiple
1293 comparisons test revealed a significant difference between WT + WT EZRIN O/E and
1294 LRRK2 G2019S$^{ki/ki}$ + WT EZRIN O/E (p = 0.0107, 95% C.I. = [-65.46, -5.94]), and between
1295 WT + Phospho-dead EZRIN O/E and LRRK2 G2019S$^{ki/ki}$ + Phospho-dead EZRIN O/E (p
1296 < 0.0001, 95% C.I. = [-78.07, -26.92]). There were no differences between WT + WT
1297 EZRIN O/E and WT + Phospho-dead EZRIN O/E (p > 0.9999, 95% C.I. = [-37.73, 23.15]),
1298 and between LRRK2 G2019S$^{ki/ki}$ + WT EZRIN O/E and LRRK2 G2019S$^{ki/ki}$ + Phospho-
1299 dead EZRIN O/E (p = 0.0610, 95% C.I. = [-48.84, 0.6819]), alpha = 0.05.

1300

1301 **REFERENCE**

1302 1 Khakh, B. S. & Sofroniew, M. V. Diversity of astrocyte functions and phenotypes
1303 in neural circuits. *Nat Neurosci* **18**, 942-952, doi:10.1038/nn.4043 (2015).

1304 2 Torres-Ceja, B. & Olsen, M. L. A closer look at astrocyte morphology: Development,
1305 heterogeneity, and plasticity at astrocyte leaflets. *Curr Opin Neurobiol* **74**, 102550,
1306 doi:10.1016/j.conb.2022.102550 (2022).

1307 3 Allen, N. J. & Lyons, D. A. Glia as architects of central nervous system formation
1308 and function. *Science* **362**, 181-185, doi:10.1126/science.aat0473 (2018).

1309 4 Eroglu, C. & Barres, B. A. Regulation of synaptic connectivity by glia. *Nature* **468**,
1310 223-231, doi:10.1038/nature09612 (2010).

1311 5 Hirrlinger, J. & Nimmerjahn, A. A perspective on astrocyte regulation of neural
1312 circuit function and animal behavior. *Glia* **70**, 1554-1580, doi:10.1002/glia.24168 (2022).

1313 6 Sofroniew, M. V. Astrocyte Reactivity: Subtypes, States, and Functions in CNS
1314 Innate Immunity. *Trends Immunol* **41**, 758-770, doi:10.1016/j.it.2020.07.004 (2020).

1315 7 di Domenico, A. *et al.* Patient-Specific iPSC-Derived Astrocytes Contribute to Non-
1316 Cell-Autonomous Neurodegeneration in Parkinson's Disease. *Stem Cell Reports* **12**, 213-
1317 229, doi:10.1016/j.stemcr.2018.12.011 (2019).

1318 8 Liddelow, S. A. *et al.* Neurotoxic reactive astrocytes are induced by activated
1319 microglia. *Nature* **541**, 481-487, doi:10.1038/nature21029 (2017).

1320 9 Saijo, K. *et al.* A Nurr1/CoREST pathway in microglia and astrocytes protects
1321 dopaminergic neurons from inflammation-induced death. *Cell* **137**, 47-59,
1322 doi:10.1016/j.cell.2009.01.038 (2009).

1323 10 Chan, C. S., Gertler, T. S. & Surmeier, D. J. Calcium homeostasis, selective
1324 vulnerability and Parkinson's disease. *Trends Neurosci* **32**, 249-256,
1325 doi:10.1016/j.tins.2009.01.006 (2009).
1326 11 Kam, T. I., Hinkle, J. T., Dawson, T. M. & Dawson, V. L. Microglia and astrocyte
1327 dysfunction in parkinson's disease. *Neurobiol Dis* **144**, 105028,
1328 doi:10.1016/j.nbd.2020.105028 (2020).
1329 12 Brandebura, A. N., Paumier, A., Onur, T. S. & Allen, N. J. Astrocyte contribution to
1330 dysfunction, risk and progression in neurodegenerative disorders. *Nat Rev Neurosci*,
1331 doi:10.1038/s41583-022-00641-1 (2022).
1332 13 Guttenplan, K. A. *et al.* Neurotoxic reactive astrocytes induce cell death via
1333 saturated lipids. *Nature* **599**, 102-107, doi:10.1038/s41586-021-03960-y (2021).
1334 14 Yun, S. P. *et al.* Block of A1 astrocyte conversion by microglia is neuroprotective
1335 in models of Parkinson's disease. *Nat Med* **24**, 931-938, doi:10.1038/s41591-018-0051-
1336 5 (2018).
1337 15 Nagai, J. *et al.* Behaviorally consequential astrocytic regulation of neural circuits.
1338 *Neuron* **109**, 576-596, doi:10.1016/j.neuron.2020.12.008 (2021).
1339 16 Lavialle, M. *et al.* Structural plasticity of perisynaptic astrocyte processes involves
1340 ezrin and metabotropic glutamate receptors. *Proc Natl Acad Sci U S A* **108**, 12915-12919,
1341 doi:10.1073/pnas.1100957108 (2011).
1342 17 Derouiche, A., Anlauf, E., Aumann, G., Muhlstadt, B. & Lavialle, M. Anatomical
1343 aspects of glia-synapse interaction: the perisynaptic glial sheath consists of a specialized
1344 astrocyte compartment. *J Physiol Paris* **96**, 177-182, doi:10.1016/s0928-4257(02)00004-
1345 9 (2002).

1346 18 Semyanov, A. & Verkhratsky, A. Astrocytic processes: from tripartite synapses to
1347 the active milieu. *Trends Neurosci* **44**, 781-792, doi:10.1016/j.tins.2021.07.006 (2021).
1348 19 Farizatto, K. L. G. & Baldwin, K. T. Astrocyte-synapse interactions during brain
1349 development. *Curr Opin Neurobiol* **80**, 102704, doi:10.1016/j.conb.2023.102704 (2023).
1350 20 Hasan, U. & Singh, S. K. The Astrocyte-Neuron Interface: An Overview on
1351 Molecular and Cellular Dynamics Controlling Formation and Maintenance of the Tripartite
1352 Synapse. *Methods Mol Biol* **1938**, 3-18, doi:10.1007/978-1-4939-9068-9_1 (2019).
1353 21 Lyon, K. A. & Allen, N. J. From Synapses to Circuits, Astrocytes Regulate Behavior.
1354 *Front Neural Circuits* **15**, 786293, doi:10.3389/fncir.2021.786293 (2021).
1355 22 Allen, N. J. & Barres, B. A. Neuroscience: Glia - more than just brain glue. *Nature*
1356 **457**, 675-677, doi:10.1038/457675a (2009).
1357 23 Murphy-Royal, C., Dupuis, J., Groc, L. & Oliet, S. H. R. Astroglial glutamate
1358 transporters in the brain: Regulating neurotransmitter homeostasis and synaptic
1359 transmission. *J Neurosci Res* **95**, 2140-2151, doi:10.1002/jnr.24029 (2017).
1360 24 Farhy-Tselnicker, I. & Allen, N. J. Astrocytes, neurons, synapses: a tripartite view
1361 on cortical circuit development. *Neural Dev* **13**, 7, doi:10.1186/s13064-018-0104-y (2018).
1362 25 Allen, N. J. & Eroglu, C. Cell Biology of Astrocyte-Synapse Interactions. *Neuron*
1363 **96**, 697-708, doi:10.1016/j.neuron.2017.09.056 (2017).
1364 26 Clavreul, S. *et al.* Cortical astrocytes develop in a plastic manner at both clonal
1365 and cellular levels. *Nat Commun* **10**, 4884, doi:10.1038/s41467-019-12791-5 (2019).
1366 27 Takano, T. *et al.* Chemico-genetic discovery of astrocytic control of inhibition in
1367 vivo. *Nature* **588**, 296-302, doi:10.1038/s41586-020-2926-0 (2020).

1368 28 Stogsdill, J. A. *et al.* Astrocytic neuroligins control astrocyte morphogenesis and
1369 synaptogenesis. *Nature* **551**, 192-197, doi:10.1038/nature24638 (2017).
1370 29 Porter, J. T. & McCarthy, K. D. Astrocytic neurotransmitter receptors in situ and in
1371 vivo. *Prog Neurobiol* **51**, 439-455, doi:10.1016/s0301-0082(96)00068-8 (1997).
1372 30 Kofuji, P. & Araque, A. G-Protein-Coupled Receptors in Astrocyte-Neuron
1373 Communication. *Neuroscience* **456**, 71-84, doi:10.1016/j.neuroscience.2020.03.025
1374 (2021).
1375 31 Tan, C. X. & Eroglu, C. Cell adhesion molecules regulating astrocyte-neuron
1376 interactions. *Curr Opin Neurobiol* **69**, 170-177, doi:10.1016/j.conb.2021.03.015 (2021).
1377 32 Holt, L. M. *et al.* Astrocyte morphogenesis is dependent on BDNF signaling via
1378 astrocytic TrkB.T1. *Elife* **8**, doi:10.7554/eLife.44667 (2019).
1379 33 Braak, H., Sastre, M. & Del Tredici, K. Development of alpha-synuclein
1380 immunoreactive astrocytes in the forebrain parallels stages of intraneuronal pathology in
1381 sporadic Parkinson's disease. *Acta Neuropathol* **114**, 231-241, doi:10.1007/s00401-007-
1382 0244-3 (2007).
1383 34 Wakabayashi, K., Hayashi, S., Yoshimoto, M., Kudo, H. & Takahashi, H.
1384 NACP/alpha-synuclein-positive filamentous inclusions in astrocytes and
1385 oligodendrocytes of Parkinson's disease brains. *Acta Neuropathol* **99**, 14-20,
1386 doi:10.1007/pl00007400 (2000).
1387 35 Tolosa, E., Garrido, A., Scholz, S. W. & Poewe, W. Challenges in the diagnosis of
1388 Parkinson's disease. *Lancet Neurol* **20**, 385-397, doi:10.1016/S1474-4422(21)00030-2
1389 (2021).

1390 36 Bloem, B. R., Okun, M. S. & Klein, C. Parkinson's disease. *Lancet* **397**, 2284-2303,
1391 doi:10.1016/S0140-6736(21)00218-X (2021).
1392 37 Kalia, L. V. & Lang, A. E. Parkinson's disease. *Lancet* **386**, 896-912,
1393 doi:10.1016/S0140-6736(14)61393-3 (2015).
1394 38 Maiti, P., Manna, J. & Dunbar, G. L. Current understanding of the molecular
1395 mechanisms in Parkinson's disease: Targets for potential treatments. *Transl*
1396 *Neurodegener* **6**, 28, doi:10.1186/s40035-017-0099-z (2017).
1397 39 Dauer, W. & Przedborski, S. Parkinson's disease: mechanisms and models.
1398 *Neuron* **39**, 889-909, doi:10.1016/s0896-6273(03)00568-3 (2003).
1399 40 Hussein, A. *et al.* Non-Motor Symptoms of Parkinson's Disease: The Neurobiology
1400 of Early Psychiatric and Cognitive Dysfunction. *Neuroscientist*, 10738584211011979,
1401 doi:10.1177/10738584211011979 (2021).
1402 41 Pachi, I. *et al.* Apathy: An underestimated feature in GBA and LRRK2 non-
1403 manifesting mutation carriers. *Parkinsonism Relat Disord* **91**, 1-8,
1404 doi:10.1016/j.parkreldis.2021.08.008 (2021).
1405 42 Weintraub, D. *et al.* The neuropsychiatry of Parkinson's disease: advances and
1406 challenges. *Lancet Neurol* **21**, 89-102, doi:10.1016/S1474-4422(21)00330-6 (2022).
1407 43 Belarbi, S. *et al.* LRRK2 G2019S mutation in Parkinson's disease: a
1408 neuropsychological and neuropsychiatric study in a large Algerian cohort. *Parkinsonism*
1409 *Relat Disord* **16**, 676-679, doi:10.1016/j.parkreldis.2010.09.003 (2010).
1410 44 Blesa, J., Foffani, G., Dehay, B., Bezard, E. & Obeso, J. A. Motor and non-motor
1411 circuit disturbances in early Parkinson disease: which happens first? *Nat Rev Neurosci*
1412 **23**, 115-128, doi:10.1038/s41583-021-00542-9 (2022).

1413 45 Foffani, G. & Obeso, J. A. A Cortical Pathogenic Theory of Parkinson's Disease.
1414 *Neuron* **99**, 1116-1128, doi:10.1016/j.neuron.2018.07.028 (2018).
1415 46 Dong, X. X., Wang, Y. & Qin, Z. H. Molecular mechanisms of excitotoxicity and
1416 their relevance to pathogenesis of neurodegenerative diseases. *Acta Pharmacol Sin* **30**,
1417 379-387, doi:10.1038/aps.2009.24 (2009).
1418 47 Booth, H. D. E., Hirst, W. D. & Wade-Martins, R. The Role of Astrocyte Dysfunction
1419 in Parkinson's Disease Pathogenesis. *Trends Neurosci* **40**, 358-370,
1420 doi:10.1016/j.tins.2017.04.001 (2017).
1421 48 Bandres-Ciga, S., Diez-Fairen, M., Kim, J. J. & Singleton, A. B. Genetics of
1422 Parkinson's disease: An introspection of its journey towards precision medicine.
1423 *Neurobiol Dis* **137**, 104782, doi:10.1016/j.nbd.2020.104782 (2020).
1424 49 Pang, S. Y. *et al.* LRRK2, GBA and their interaction in the regulation of autophagy:
1425 implications on therapeutics in Parkinson's disease. *Transl Neurodegener* **11**, 5,
1426 doi:10.1186/s40035-022-00281-6 (2022).
1427 50 Udayar, V., Chen, Y., Sidransky, E. & Jagasia, R. Lysosomal dysfunction in
1428 neurodegeneration: emerging concepts and methods. *Trends Neurosci* **45**, 184-199,
1429 doi:10.1016/j.tins.2021.12.004 (2022).
1430 51 Najafi, S. *et al.* Recent insights into the roles of circular RNAs in human brain
1431 development and neurologic diseases. *Int J Biol Macromol*,
1432 doi:10.1016/j.ijbiomac.2022.11.166 (2022).
1433 52 Zhang, Y. *et al.* Purification and Characterization of Progenitor and Mature Human
1434 Astrocytes Reveals Transcriptional and Functional Differences with Mouse. *Neuron* **89**,
1435 37-53, doi:10.1016/j.neuron.2015.11.013 (2016).

1436 53 Uhlen, M. *et al.* Proteomics. Tissue-based map of the human proteome. *Science*
1437 **347**, 1260419, doi:10.1126/science.1260419 (2015).
1438 54 Digre, A. & Lindskog, C. The Human Protein Atlas-Spatial localization of the
1439 human proteome in health and disease. *Protein Sci* **30**, 218-233, doi:10.1002/pro.3987
1440 (2021).
1441 55 Gilks, W. P. *et al.* A common LRRK2 mutation in idiopathic Parkinson's disease.
1442 *Lancet* **365**, 415-416, doi:10.1016/S0140-6736(05)17830-1 (2005).
1443 56 Benamer, H. T. The ancestry of LRRK2 Gly2019Ser parkinsonism. *Lancet Neurol*
1444 **7**, 769-770; author reply 770-761, doi:10.1016/S1474-4422(08)70178-9 (2008).
1445 57 Ren, C. *et al.* G2019S Variation in LRRK2: An Ideal Model for the Study of
1446 Parkinson's Disease? *Front Hum Neurosci* **13**, 306, doi:10.3389/fnhum.2019.00306
1447 (2019).
1448 58 West, A. B. *et al.* Parkinson's disease-associated mutations in leucine-rich repeat
1449 kinase 2 augment kinase activity. *Proc Natl Acad Sci U S A* **102**, 16842-16847,
1450 doi:10.1073/pnas.0507360102 (2005).
1451 59 Greggio, E. *et al.* Kinase activity is required for the toxic effects of mutant
1452 LRRK2/dardarin. *Neurobiol Dis* **23**, 329-341, doi:10.1016/j.nbd.2006.04.001 (2006).
1453 60 Jaleel, M. *et al.* LRRK2 phosphorylates moesin at threonine-558: characterization
1454 of how Parkinson's disease mutants affect kinase activity. *Biochem J* **405**, 307-317,
1455 doi:10.1042/BJ20070209 (2007).
1456 61 Ito, G. *et al.* Phos-tag analysis of Rab10 phosphorylation by LRRK2: a powerful
1457 assay for assessing kinase function and inhibitors. *Biochem J* **473**, 2671-2685,
1458 doi:10.1042/BCJ20160557 (2016).

1459 62 Steger, M. *et al.* Systematic proteomic analysis of LRRK2-mediated Rab GTPase
1460 phosphorylation establishes a connection to ciliogenesis. *Elife* **6**, doi:10.7554/eLife.31012
1461 (2017).
1462 63 Steger, M. *et al.* Phosphoproteomics reveals that Parkinson's disease kinase
1463 LRRK2 regulates a subset of Rab GTPases. *Elife* **5**, doi:10.7554/eLife.12813 (2016).
1464 64 Kluss, J. H., Mamais, A. & Cookson, M. R. LRRK2 links genetic and sporadic
1465 Parkinson's disease. *Biochem Soc Trans* **47**, 651-661, doi:10.1042/BST20180462 (2019).
1466 65 Monfrini, E. & Di Fonzo, A. Leucine-Rich Repeat Kinase (LRRK2) Genetics and
1467 Parkinson's Disease. *Adv Neurobiol* **14**, 3-30, doi:10.1007/978-3-319-49969-7_1 (2017).
1468 66 Mestre, T. A. *et al.* Clustering of motor and nonmotor traits in leucine-rich repeat
1469 kinase 2 G2019S Parkinson's disease nonparkinsonian relatives: A multicenter family
1470 study. *Mov Disord* **33**, 960-965, doi:10.1002/mds.27272 (2018).
1471 67 Chang, E. E. S. *et al.* LRRK2 mutant knock-in mouse models: therapeutic
1472 relevance in Parkinson's disease. *Translational Neurodegeneration* **11**, doi:ARTN 10

1473 10.1186/s40035-022-00285-2 (2022).
1474 68 Yue, M. *et al.* Progressive dopaminergic alterations and mitochondrial
1475 abnormalities in LRRK2 G2019S knock-in mice. *Neurobiol Dis* **78**, 172-195,
1476 doi:10.1016/j.nbd.2015.02.031 (2015).
1477 69 Longo, F. *et al.* Age-dependent dopamine transporter dysfunction and Serine129
1478 phospho-alpha-synuclein overload in G2019S LRRK2 mice. *Acta Neuropathol Commun*
1479 **5**, 22, doi:10.1186/s40478-017-0426-8 (2017).

1480 70 Narayanan, N. S., Rodnitzky, R. L. & Uc, E. Y. Prefrontal dopamine signaling and
1481 cognitive symptoms of Parkinson's disease. *Rev Neurosci* **24**, 267-278,
1482 doi:10.1515/revneuro-2013-0004 (2013).
1483 71 Cousineau, J., Plateau, V., Baufreton, J. & Le Bon-Jego, M. Dopaminergic
1484 modulation of primary motor cortex: From cellular and synaptic mechanisms underlying
1485 motor learning to cognitive symptoms in Parkinson's disease. *Neurobiol Dis* **167**, 105674,
1486 doi:10.1016/j.nbd.2022.105674 (2022).
1487 72 Volta, M. & Melrose, H. LRRK2 mouse models: dissecting the behavior, striatal
1488 neurochemistry and neurophysiology of PD pathogenesis. *Biochem Soc Trans* **45**, 113-
1489 122, doi:10.1042/BST20160238 (2017).
1490 73 Vingill, S., Connor-Robson, N. & Wade-Martins, R. Are rodent models of
1491 Parkinson's disease behaving as they should? *Behav Brain Res* **352**, 133-141,
1492 doi:10.1016/j.bbr.2017.10.021 (2018).
1493 74 Hussein, A., Tielemans, A., Baxter, M. G., Benson, D. L. & Huntley, G. W.
1494 Cognitive deficits and altered cholinergic innervation in young adult male mice carrying a
1495 Parkinson's disease Lrrk2(G2019S) knockin mutation. *Exp Neurol* **355**, 114145,
1496 doi:10.1016/j.expneurol.2022.114145 (2022).
1497 75 Guevara, C. A. *et al.* LRRK2 mutation alters behavioral, synaptic, and nonsynaptic
1498 adaptations to acute social stress. *J Neurophysiol* **123**, 2382-2389,
1499 doi:10.1152/jn.00137.2020 (2020).
1500 76 Matikainen-Ankney, B. A. *et al.* Parkinson's Disease-Linked LRRK2-G2019S
1501 Mutation Alters Synaptic Plasticity and Promotes Resilience to Chronic Social Stress in

1502 Young Adulthood. *J Neurosci* **38**, 9700-9711, doi:10.1523/JNEUROSCI.1457-18.2018
1503 (2018).
1504 77 Chen, C. *et al.* Pathway-specific dysregulation of striatal excitatory synapses by
1505 LRRK2 mutations. *Elife* **9**, doi:10.7554/eLife.58997 (2020).
1506 78 Kuhlmann, N. & Milnerwood, A. J. A Critical LRRK at the Synapse? The
1507 Neurobiological Function and Pathophysiological Dysfunction of LRRK2. *Front Mol*
1508 *Neurosci* **13**, 153, doi:10.3389/fnmol.2020.00153 (2020).
1509 79 Lim, J. *et al.* LRRK2 G2019S Induces Anxiety/Depression-like Behavior before the
1510 Onset of Motor Dysfunction with 5-HT(1A) Receptor Upregulation in Mice. *J Neurosci* **38**,
1511 1611-1621, doi:10.1523/JNEUROSCI.4051-15.2017 (2018).
1512 80 Arbez, N. *et al.* G2019S-LRRK2 mutation enhances MPTP-linked Parkinsonism in
1513 mice. *Hum Mol Genet* **29**, 580-590, doi:10.1093/hmg/ddz271 (2020).
1514 81 Skiteva, O., Yao, N., Sitzia, G. & Chergui, K. LRRK2-G2019S mice display
1515 alterations in glutamatergic synaptic transmission in midbrain dopamine neurons. *J*
1516 *Neurochem* **161**, 158-172, doi:10.1111/jnc.15588 (2022).
1517 82 Lawal, O., Ulloa Severino, F. P. & Eroglu, C. The role of astrocyte structural
1518 plasticity in regulating neural circuit function and behavior. *Glia* **70**, 1467-1483,
1519 doi:10.1002/glia.24191 (2022).
1520 83 Shani, V. *et al.* Physiological and pathological roles of LRRK2 in the nuclear
1521 envelope integrity. *Hum Mol Genet* **28**, 3982-3996, doi:10.1093/hmg/ddz245 (2019).
1522 84 Heaton, G. R. *et al.* Sequential screening nominates the Parkinson's disease
1523 associated kinase LRRK2 as a regulator of Clathrin-mediated endocytosis. *Neurobiol Dis*
1524 **141**, 104948, doi:10.1016/j.nbd.2020.104948 (2020).

1525 85 Matikainen-Ankney, B. A. *et al.* Altered Development of Synapse Structure and
1526 Function in Striatum Caused by Parkinson's Disease-Linked LRRK2-G2019S Mutation. *J*
1527 *Neurosci* **36**, 7128-7141, doi:10.1523/JNEUROSCI.3314-15.2016 (2016).
1528 86 Baldwin, K. T. *et al.* HepaCAM controls astrocyte self-organization and coupling.
1529 *Neuron* **109**, 2427-2442 e2410, doi:10.1016/j.neuron.2021.05.025 (2021).
1530 87 Baptista, M. A. *et al.* Loss of leucine-rich repeat kinase 2 (LRRK2) in rats leads to
1531 progressive abnormal phenotypes in peripheral organs. *PLoS One* **8**, e80705,
1532 doi:10.1371/journal.pone.0080705 (2013).
1533 88 Ness, D. *et al.* Leucine-rich repeat kinase 2 (LRRK2)-deficient rats exhibit renal
1534 tubule injury and perturbations in metabolic and immunological homeostasis. *PLoS One*
1535 **8**, e66164, doi:10.1371/journal.pone.0066164 (2013).
1536 89 Daher, J. P., Volpicelli-Daley, L. A., Blackburn, J. P., Moehle, M. S. & West, A. B.
1537 Abrogation of alpha-synuclein-mediated dopaminergic neurodegeneration in LRRK2-
1538 deficient rats. *Proc Natl Acad Sci U S A* **111**, 9289-9294, doi:10.1073/pnas.1403215111
1539 (2014).
1540 90 Miklavc, P. *et al.* Surfactant secretion in LRRK2 knock-out rats: changes in lamellar
1541 body morphology and rate of exocytosis. *PLoS One* **9**, e84926,
1542 doi:10.1371/journal.pone.0084926 (2014).
1543 91 Taylor, M. & Alessi, D. R. Advances in elucidating the function of leucine-rich
1544 repeat protein kinase-2 in normal cells and Parkinson's disease. *Curr Opin Cell Biol* **63**,
1545 102-113, doi:10.1016/j.ceb.2020.01.001 (2020).
1546 92 Bonet-Ponce, L. & Cookson, M. R. LRRK2 recruitment, activity, and function in
1547 organelles. *FEBS J* **289**, 6871-6890, doi:10.1111/febs.16099 (2022).

1548 93 Jeong, G. R. *et al.* Dysregulated phosphorylation of Rab GTPases by LRRK2
1549 induces neurodegeneration. *Mol Neurodegener* **13**, 8, doi:10.1186/s13024-018-0240-1
1550 (2018).
1551 94 Arranz, A. M. *et al.* LRRK2 functions in synaptic vesicle endocytosis through a
1552 kinase-dependent mechanism. *J Cell Sci* **128**, 541-552, doi:10.1242/jcs.158196 (2015).
1553 95 Martin, I. *et al.* Ribosomal protein s15 phosphorylation mediates LRRK2
1554 neurodegeneration in Parkinson's disease. *Cell* **157**, 472-485,
1555 doi:10.1016/j.cell.2014.01.064 (2014).
1556 96 Belluzzi, E. *et al.* LRRK2 phosphorylates pre-synaptic N-ethylmaleimide sensitive
1557 fusion (NSF) protein enhancing its ATPase activity and SNARE complex disassembling
1558 rate. *Mol Neurodegener* **11**, 1, doi:10.1186/s13024-015-0066-z (2016).
1559 97 Islam, M. S. *et al.* Human R1441C LRRK2 regulates the synaptic vesicle proteome
1560 and phosphoproteome in a Drosophila model of Parkinson's disease. *Hum Mol Genet* **25**,
1561 5365-5382, doi:10.1093/hmg/ddw352 (2016).
1562 98 Kalogeropulou, A. F. *et al.* P62/SQSTM1 is a novel leucine-rich repeat kinase 2
1563 (LRRK2) substrate that enhances neuronal toxicity. *Biochem J* **475**, 1271-1293,
1564 doi:10.1042/BCJ20170699 (2018).
1565 99 Nguyen, M. & Krainc, D. LRRK2 phosphorylation of auxilin mediates synaptic
1566 defects in dopaminergic neurons from patients with Parkinson's disease. *Proc Natl Acad*
1567 *Sci U S A* **115**, 5576-5581, doi:10.1073/pnas.1717590115 (2018).
1568 100 Dhekne, H. S. *et al.* A pathway for Parkinson's Disease LRRK2 kinase to block
1569 primary cilia and Sonic hedgehog signaling in the brain. *Elife* **7**, doi:10.7554/eLife.40202
1570 (2018).

1571 101 Lara Ordonez, A. J. *et al.* RAB8, RAB10 and RILPL1 contribute to both LRRK2
1572 kinase-mediated centrosomal cohesion and ciliogenesis deficits. *Hum Mol Genet* **28**,
1573 3552-3568, doi:10.1093/hmg/ddz201 (2019).
1574 102 Waschbusch, D. *et al.* Structural Basis for Rab8a Recruitment of RILPL2 via
1575 LRRK2 Phosphorylation of Switch 2. *Structure* **28**, 406-417 e406,
1576 doi:10.1016/j.str.2020.01.005 (2020).
1577 103 Gomez, R. C., Wawro, P., Lis, P., Alessi, D. R. & Pfeffer, S. R. Membrane
1578 association but not identity is required for LRRK2 activation and phosphorylation of Rab
1579 GTPases. *J Cell Biol* **218**, 4157-4170, doi:10.1083/jcb.201902184 (2019).
1580 104 Herbst, S. *et al.* LRRK2 activation controls the repair of damaged endomembranes
1581 in macrophages. *EMBO J* **39**, e104494, doi:10.15252/embj.2020104494 (2020).
1582 105 Lee, H. *et al.* LRRK2 Is Recruited to Phagosomes and Co-recruits RAB8 and
1583 RAB10 in Human Pluripotent Stem Cell-Derived Macrophages. *Stem Cell Reports* **14**,
1584 940-955, doi:10.1016/j.stemcr.2020.04.001 (2020).
1585 106 Thiele, D. L. & Lipsky, P. E. Mechanism of L-leucyl-L-leucine methyl ester-
1586 mediated killing of cytotoxic lymphocytes: dependence on a lysosomal thiol protease,
1587 dipeptidyl peptidase I, that is enriched in these cells. *Proc Natl Acad Sci U S A* **87**, 83-87,
1588 doi:10.1073/pnas.87.1.83 (1990).
1589 107 Takagawa, T. *et al.* An increase in LRRK2 suppresses autophagy and enhances
1590 Dectin-1-induced immunity in a mouse model of colitis. *Sci Transl Med* **10**,
1591 doi:10.1126/scitranslmed.aan8162 (2018).

1592 108 Shutinoski, B. *et al.* Lrrk2 alleles modulate inflammation during microbial infection
1593 of mice in a sex-dependent manner. *Sci Transl Med* **11**,
1594 doi:10.1126/scitranslmed.aas9292 (2019).
1595 109 Bonello, F. *et al.* LRRK2 impairs PINK1/Parkin-dependent mitophagy via its kinase
1596 activity: pathologic insights into Parkinson's disease. *Hum Mol Genet* **28**, 1645-1660,
1597 doi:10.1093/hmg/ddz004 (2019).
1598 110 Gan, L., Cookson, M. R., Petrucelli, L. & La Spada, A. R. Converging pathways in
1599 neurodegeneration, from genetics to mechanisms. *Nat Neurosci* **21**, 1300-1309,
1600 doi:10.1038/s41593-018-0237-7 (2018).
1601 111 Korecka, J. A. *et al.* Mitochondrial clearance and maturation of autophagosomes
1602 are compromised in LRRK2 G2019S familial Parkinson's disease patient fibroblasts. *Hum*
1603 *Mol Genet* **28**, 3232-3243, doi:10.1093/hmg/ddz126 (2019).
1604 112 Hsieh, C. H. *et al.* Functional Impairment in Miro Degradation and Mitophagy Is a
1605 Shared Feature in Familial and Sporadic Parkinson's Disease. *Cell Stem Cell* **19**, 709-
1606 724, doi:10.1016/j.stem.2016.08.002 (2016).
1607 113 Toyofuku, T., Okamoto, Y., Ishikawa, T., Sasawatari, S. & Kumanogoh, A. LRRK2
1608 regulates endoplasmic reticulum-mitochondrial tethering through the PERK-mediated
1609 ubiquitination pathway. *EMBO J* **39**, e100875, doi:10.15252/embj.2018100875 (2020).
1610 114 Inoshita, T. *et al.* Vps35 in cooperation with LRRK2 regulates synaptic vesicle
1611 endocytosis through the endosomal pathway in Drosophila. *Hum Mol Genet* **26**, 2933-
1612 2948, doi:10.1093/hmg/ddx179 (2017).
1613 115 Hur, E. M., Jang, E. H., Jeong, G. R. & Lee, B. D. LRRK2 and membrane trafficking:
1614 nexus of Parkinson's disease. *BMB Rep* **52**, 533-539 (2019).

1615 116 Parisiadou, L. *et al.* Phosphorylation of ezrin/radixin/moesin proteins by LRRK2
1616 promotes the rearrangement of actin cytoskeleton in neuronal morphogenesis. *J Neurosci*
1617 **29**, 13971-13980, doi:10.1523/JNEUROSCI.3799-09.2009 (2009).
1618 117 Parisiadou, L. & Cai, H. LRRK2 function on actin and microtubule dynamics in
1619 Parkinson disease. *Commun Integr Biol* **3**, 396-400, doi:10.4161/cib.3.5.12286 (2010).
1620 118 Bretscher, A., Edwards, K. & Fehon, R. G. ERM proteins and merlin: integrators at
1621 the cell cortex. *Nat Rev Mol Cell Biol* **3**, 586-599, doi:10.1038/nrm882 (2002).
1622 119 Gautreau, A., Louvard, D. & Arpin, M. Morphogenic effects of ezrin require a
1623 phosphorylation-induced transition from oligomers to monomers at the plasma membrane.
1624 *J Cell Biol* **150**, 193-203, doi:10.1083/jcb.150.1.193 (2000).
1625 120 Zhu, L. *et al.* High turnover of ezrin T567 phosphorylation: conformation, activity,
1626 and cellular function. *Am J Physiol Cell Physiol* **293**, C874-884,
1627 doi:10.1152/ajpcell.00111.2007 (2007).
1628 121 Endo, F. *et al.* Molecular basis of astrocyte diversity and morphology across the
1629 CNS in health and disease. *Science* **378**, eadc9020, doi:10.1126/science.adc9020 (2022).
1630 122 Kruyer, A., Scofield, M. D., Wood, D., Reissner, K. J. & Kalivas, P. W. Heroin Cue-
1631 Evoked Astrocytic Structural Plasticity at Nucleus Accumbens Synapses Inhibits Heroin
1632 Seeking. *Biol Psychiatry* **86**, 811-819, doi:10.1016/j.biopsych.2019.06.026 (2019).
1633 123 Schacke, S. *et al.* Ezrin deficiency triggers glial fibrillary acidic protein upregulation
1634 and a distinct reactive astrocyte phenotype. *Glia* **70**, 2309-2329, doi:10.1002/glia.24253
1635 (2022).
1636 124 Zaman, R. *et al.* Effector-mediated ERM activation locally inhibits RhoA activity to
1637 shape the apical cell domain. *J Cell Biol* **220**, doi:10.1083/jcb.202007146 (2021).

1638 125 Tsai, F. C. *et al.* Ezrin enrichment on curved membranes requires a specific
1639 conformation or interaction with a curvature-sensitive partner. *Elife* **7**,
1640 doi:10.7554/eLife.37262 (2018).
1641 126 Viswanatha, R., Ohouo, P. Y., Smolka, M. B. & Bretscher, A. Local phosphocycling
1642 mediated by LOK/SLK restricts ezrin function to the apical aspect of epithelial cells. *J Cell*
1643 *Biol* **199**, 969-984, doi:10.1083/jcb.201207047 (2012).
1644 127 Korkmazhan, E. & Dunn, A. R. The membrane-actin linker ezrin acts as a sliding
1645 anchor. *Sci Adv* **8**, eabo2779, doi:10.1126/sciadv.abo2779 (2022).
1646 128 Keo, A. *et al.* Cingulate networks associated with gray matter loss in Parkinson's
1647 disease show high expression of cholinergic genes in the healthy brain. *Eur J Neurosci*
1648 **53**, 3727-3739, doi:10.1111/ejn.15216 (2021).
1649 129 Carbon, M., Felice Ghilardi, M., Dhawan, V. & Eidelberg, D. Correlates of
1650 movement initiation and velocity in Parkinson's disease: A longitudinal PET study.
1651 *Neuroimage* **34**, 361-370, doi:10.1016/j.neuroimage.2006.08.019 (2007).
1652 130 Ranchet, M. *et al.* Changes in Prefrontal Cortical Activity During Walking and
1653 Cognitive Functions Among Patients With Parkinson's Disease. *Front Neurol* **11**, 601686,
1654 doi:10.3389/fneur.2020.601686 (2020).
1655 131 Oberheim, N. A. *et al.* Uniquely hominid features of adult human astrocytes. *J*
1656 *Neurosci* **29**, 3276-3287, doi:10.1523/JNEUROSCI.4707-08.2009 (2009).
1657 132 Freeman, M. R. Specification and morphogenesis of astrocytes. *Science* **330**, 774-
1658 778, doi:10.1126/science.1190928 (2010).

1659 133 Baldwin, K. T. & Eroglu, C. Molecular mechanisms of astrocyte-induced
1660 synaptogenesis. *Curr Opin Neurobiol* **45**, 113-120, doi:10.1016/j.conb.2017.05.006
1661 (2017).
1662 134 Beccano-Kelly, D. A. *et al.* LRRK2 overexpression alters glutamatergic presynaptic
1663 plasticity, striatal dopamine tone, postsynaptic signal transduction, motor activity and
1664 memory. *Hum Mol Genet* **24**, 1336-1349, doi:10.1093/hmg/ddu543 (2015).
1665 135 Piccoli, G. *et al.* LRRK2 controls synaptic vesicle storage and mobilization within
1666 the recycling pool. *J Neurosci* **31**, 2225-2237, doi:10.1523/JNEUROSCI.3730-10.2011
1667 (2011).
1668 136 Parisiadou, L. *et al.* LRRK2 regulates synaptogenesis and dopamine receptor
1669 activation through modulation of PKA activity. *Nat Neurosci* **17**, 367-376,
1670 doi:10.1038/nn.3636 (2014).
1671 137 Ponzo, V. *et al.* Impaired intracortical transmission in G2019S leucine rich-repeat
1672 kinase Parkinson patients. *Mov Disord* **32**, 750-756, doi:10.1002/mds.26931 (2017).
1673 138 West, A. B. *et al.* Differential LRRK2 expression in the cortex, striatum, and
1674 substantia nigra in transgenic and nontransgenic rodents. *J Comp Neurol* **522**, 2465-2480,
1675 doi:10.1002/cne.23583 (2014).
1676 139 Botta-Orfila, T. *et al.* Microarray expression analysis in idiopathic and LRRK2-
1677 associated Parkinson's disease. *Neurobiol Dis* **45**, 462-468,
1678 doi:10.1016/j.nbd.2011.08.033 (2012).
1679 140 Helmich, R. C. *et al.* Reorganization of corticostriatal circuits in healthy G2019S
1680 LRRK2 carriers. *Neurology* **84**, 399-406, doi:10.1212/WNL.0000000000001189 (2015).

1681 141 Skelton, P. D., Tokars, V. & Parisiadou, L. LRRK2 at Striatal Synapses: Cell-Type
1682 Specificity and Mechanistic Insights. *Cells* **11**, doi:10.3390/cells11010169 (2022).
1683 142 Kaneko, T. & Fujiyama, F. Complementary distribution of vesicular glutamate
1684 transporters in the central nervous system. *Neurosci Res* **42**, 243-250,
1685 doi:10.1016/s0168-0102(02)00009-3 (2002).
1686 143 Fremeau, R. T., Jr. *et al.* The expression of vesicular glutamate transporters
1687 defines two classes of excitatory synapse. *Neuron* **31**, 247-260, doi:10.1016/s0896-
1688 6273(01)00344-0 (2001).
1689 144 Micheva, K. D., Busse, B., Weiler, N. C., O'Rourke, N. & Smith, S. J. Single-
1690 synapse analysis of a diverse synapse population: proteomic imaging methods and
1691 markers. *Neuron* **68**, 639-653, doi:10.1016/j.neuron.2010.09.024 (2010).
1692 145 Chaudhry, F. A. *et al.* The vesicular GABA transporter, VGAT, localizes to synaptic
1693 vesicles in sets of glycinergic as well as GABAergic neurons. *J Neurosci* **18**, 9733-9750,
1694 doi:10.1523/JNEUROSCI.18-23-09733.1998 (1998).
1695 146 Tyagarajan, S. K. & Fritschy, J. M. Gephyrin: a master regulator of neuronal
1696 function? *Nat Rev Neurosci* **15**, 141-156, doi:10.1038/nrn3670 (2014).
1697 147 Ippolito, D. M. & Eroglu, C. Quantifying synapses: an immunocytochemistry-based
1698 assay to quantify synapse number. *J Vis Exp*, doi:10.3791/2270 (2010).
1699 148 Glasgow, S. D., McPhedrain, R., Madranges, J. F., Kennedy, T. E. & Ruthazer, E.
1700 S. Approaches and Limitations in the Investigation of Synaptic Transmission and
1701 Plasticity. *Front Synaptic Neurosci* **11**, 20, doi:10.3389/fnsyn.2019.00020 (2019).

1702 149 Matsuzaki, M. *et al.* Dendritic spine geometry is critical for AMPA receptor
1703 expression in hippocampal CA1 pyramidal neurons. *Nat Neurosci* **4**, 1086-1092,
1704 doi:10.1038/nn736 (2001).
1705 150 Thaler, A. *et al.* Lower cognitive performance in healthy G2019S LRRK2 mutation
1706 carriers. *Neurology* **79**, 1027-1032, doi:10.1212/WNL.0b013e3182684646 (2012).
1707 151 Simuni, T. *et al.* Clinical and dopamine transporter imaging characteristics of non-
1708 manifest LRRK2 and GBA mutation carriers in the Parkinson's Progression Markers
1709 Initiative (PPMI): a cross-sectional study. *Lancet Neurol* **19**, 71-80, doi:10.1016/S1474-
1710 4422(19)30319-9 (2020).
1711 152 Thaler, A. *et al.* Altered reward-related neural responses in non-manifesting
1712 carriers of the Parkinson disease related LRRK2 mutation. *Brain Imaging Behav* **13**,
1713 1009-1020, doi:10.1007/s11682-018-9920-2 (2019).
1714 153 Xenias, H. S. *et al.* R1441C and G2019S LRRK2 knockin mice have distinct striatal
1715 molecular, physiological, and behavioral alterations. *Commun Biol* **5**, 1211,
1716 doi:10.1038/s42003-022-04136-8 (2022).
1717 154 Schweimer, J. & Hauber, W. Involvement of the rat anterior cingulate cortex in
1718 control of instrumental responses guided by reward expectancy. *Learn Mem* **12**, 334-342,
1719 doi:10.1101/lm.90605 (2005).
1720 155 Schweimer, J. & Hauber, W. Dopamine D1 receptors in the anterior cingulate
1721 cortex regulate effort-based decision making. *Learn Mem* **13**, 777-782,
1722 doi:10.1101/lm.409306 (2006).

1723 156 Shenhav, A., Botvinick, M. M. & Cohen, J. D. The expected value of control: an
1724 integrative theory of anterior cingulate cortex function. *Neuron* **79**, 217-240,
1725 doi:10.1016/j.neuron.2013.07.007 (2013).
1726 157 Hart, E. E., Blair, G. J., O'Dell, T. J., Blair, H. T. & Izquierdo, A. Chemogenetic
1727 Modulation and Single-Photon Calcium Imaging in Anterior Cingulate Cortex Reveal a
1728 Mechanism for Effort-Based Decisions. *J Neurosci* **40**, 5628-5643,
1729 doi:10.1523/JNEUROSCI.2548-19.2020 (2020).
1730 158 Tervo, D. G. R. *et al.* The anterior cingulate cortex directs exploration of alternative
1731 strategies. *Neuron* **109**, 1876-1887 e1876, doi:10.1016/j.neuron.2021.03.028 (2021).
1732 159 Brockett, A. T., Tennyson, S. S., deBettencourt, C. A., Gaye, F. & Roesch, M. R.
1733 Anterior cingulate cortex is necessary for adaptation of action plans. *Proc Natl Acad Sci*
1734 *U S A* **117**, 6196-6204, doi:10.1073/pnas.1919303117 (2020).
1735 160 Tan, C. X., Burrus Lane, C. J. & Eroglu, C. Role of astrocytes in synapse formation
1736 and maturation. *Curr Top Dev Biol* **142**, 371-407, doi:10.1016/bs.ctdb.2020.12.010
1737 (2021).
1738 161 Pelaseyed, T. & Bretscher, A. Regulation of actin-based apical structures on
1739 epithelial cells. *J Cell Sci* **131**, doi:10.1242/jcs.221853 (2018).
1740 162 Pelaseyed, T. *et al.* Ezrin activation by LOK phosphorylation involves a PIP(2)-
1741 dependent wedge mechanism. *Elife* **6**, doi:10.7554/eLife.22759 (2017).
1742 163 Lombardo, A. T., Mitchell, C. A. R., Zaman, R., McDermitt, D. J. & Bretscher, A.
1743 ARHGAP18-Ezrin functions as a RhoA autoregulatory module in the organization of
1744 apical microvilli. *bioRxiv*, 2022.2009.2012.507663, doi:10.1101/2022.09.12.507663
1745 (2022).

1746 164 Broadhead, M. J. *et al.* Selective vulnerability of tripartite synapses in amyotrophic
1747 lateral sclerosis. *Acta Neuropathol* **143**, 471-486, doi:10.1007/s00401-022-02412-9
1748 (2022).
1749 165 Moffat, J. *et al.* A lentiviral RNAi library for human and mouse genes applied to an
1750 arrayed viral high-content screen. *Cell* **124**, 1283-1298, doi:10.1016/j.cell.2006.01.040
1751 (2006).
1752 166 Chih, B., Gollan, L. & Scheiffele, P. Alternative splicing controls selective trans-
1753 synaptic interactions of the neuroligin-neurexin complex. *Neuron* **51**, 171-178,
1754 doi:10.1016/j.neuron.2006.06.005 (2006).
1755 167 Chen, F. & LoTurco, J. A method for stable transgenesis of radial glia lineage in
1756 rat neocortex by piggyBac mediated transposition. *J Neurosci Methods* **207**, 172-180,
1757 doi:10.1016/j.jneumeth.2012.03.016 (2012).
1758 168 O'Neil, S. D. *et al.* Action potential-coupled Rho GTPase signaling drives
1759 presynaptic plasticity. *Elife* **10**, doi:10.7554/eLife.63756 (2021).
1760 169 Ferreira, T. A. *et al.* Neuronal morphometry directly from bitmap images. *Nat*
1761 *Methods* **11**, 982-984, doi:10.1038/nmeth.3125 (2014).
1762 170 Uezu, A. *et al.* Identification of an elaborate complex mediating postsynaptic
1763 inhibition. *Science* **353**, 1123-1129, doi:10.1126/science.aag0821 (2016).
1764 171 Risher, W. C. *et al.* Thrombospondin receptor alpha2delta-1 promotes
1765 synaptogenesis and spinogenesis via postsynaptic Rac1. *J Cell Biol* **217**, 3747-3765,
1766 doi:10.1083/jcb.201802057 (2018).

1767 172 Zhang, Y. *et al.* An RNA-sequencing transcriptome and splicing database of glia,
1768 neurons, and vascular cells of the cerebral cortex. *J Neurosci* **34**, 11929-11947,
1769 doi:10.1523/JNEUROSCI.1860-14.2014 (2014).

1770

Figure 1. Wang et al.,

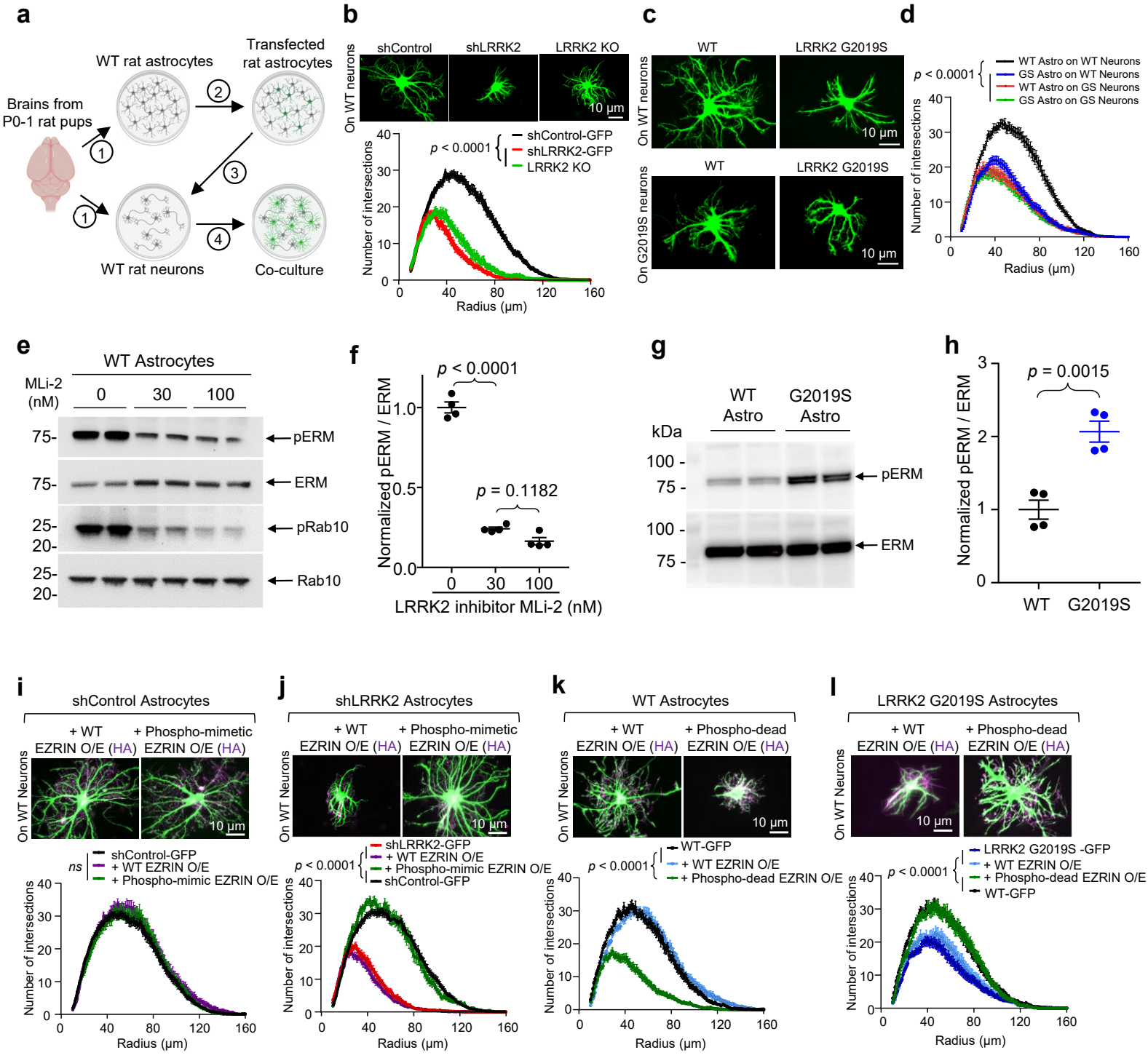

Figure 2. Wang et al.,

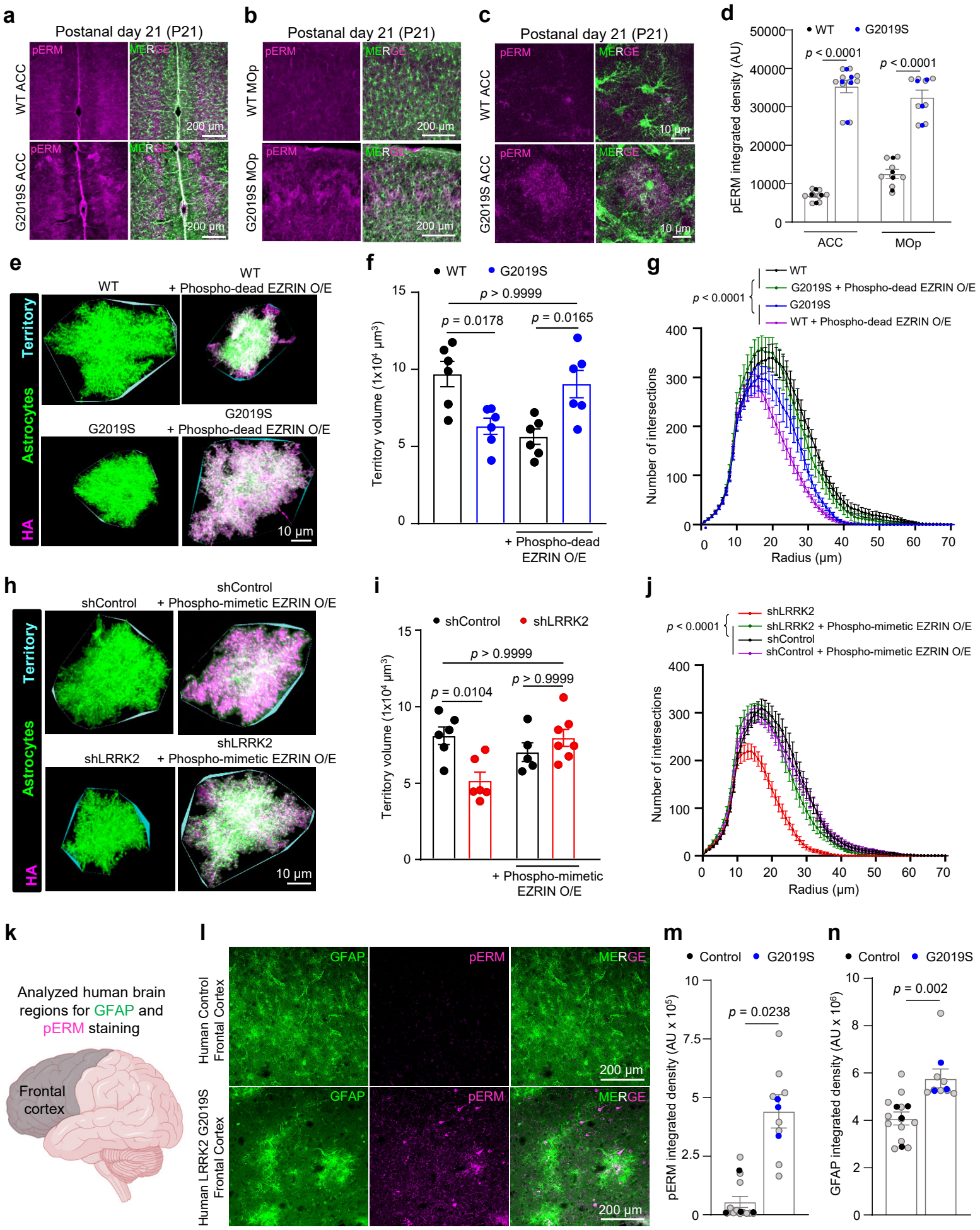

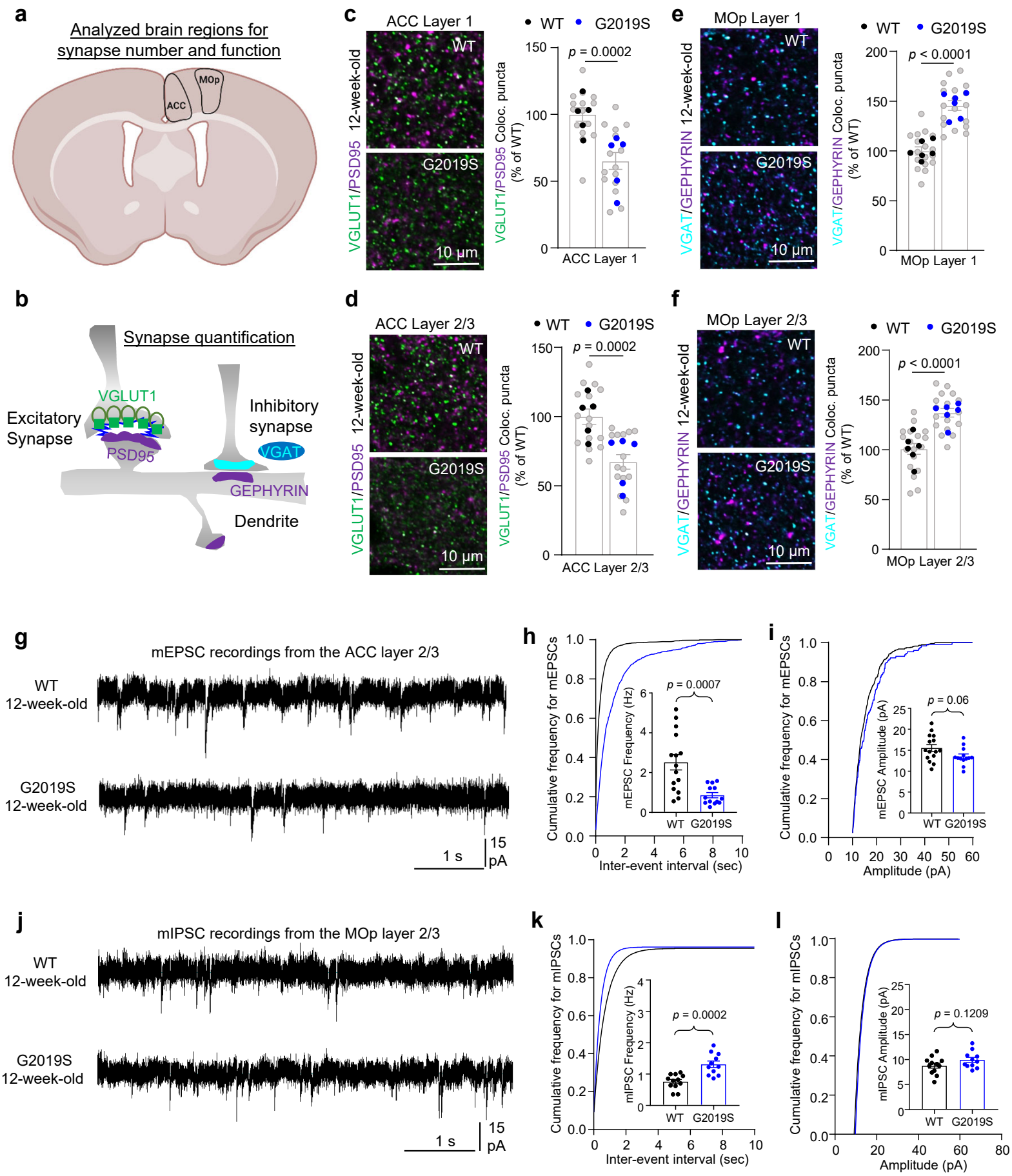
a
Analyzed brain regions for synapse number and function
ACC
MOp
b
Synapse quantification
VGLUT1
Excitatory Synapse
PSD95
Inhibitory synapse
VGAT
GEPHYRIN
Dendrite
c
ACC Layer 1
WT
G2019S
12-week-old
VGLUT1/PSD95
10 µm
VGLUT1/PSD95 Coloc. puncta (% of WT)
p = 0.0002
ACC Layer 1
d
ACC Layer 2/3
p = 0.0002
ACC Layer 2/3
e
MOp Layer 1
VGAT/GEPHYRIN
p < 0.0001
MOp Layer 1
f
MOp Layer 2/3
p < 0.0001
MOp Layer 2/3
g
mEPSC recordings from the ACC layer 2/3
WT 12-week-old
G2019S 12-week-old
1 s
15 pA
h
Cumulative frequency for mEPSCs
mEPSC Frequency (Hz)
p = 0.0007
Inter-event interval (sec)
i
mEPSC Amplitude (pA)
p = 0.06
Amplitude (pA)
j
mIPSC recordings from the MOp layer 2/3
k
Cumulative frequency for mIPSCs
mIPSC Frequency (Hz)
p = 0.0002
l
mIPSC Amplitude (pA)
p = 0.1209

Figure 4. Wang et al.,

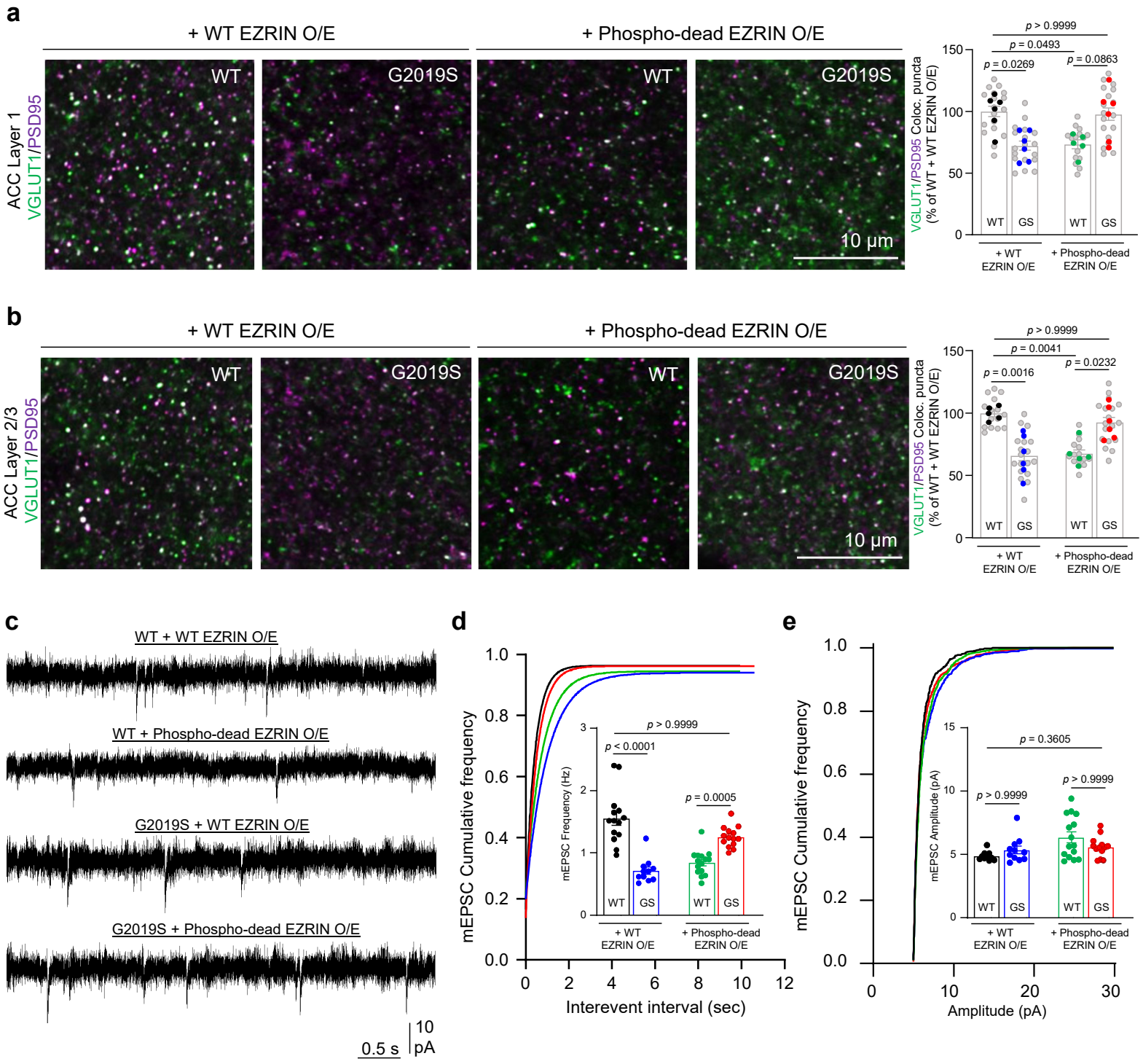

Extended Data Figure 1. Wang et al.,

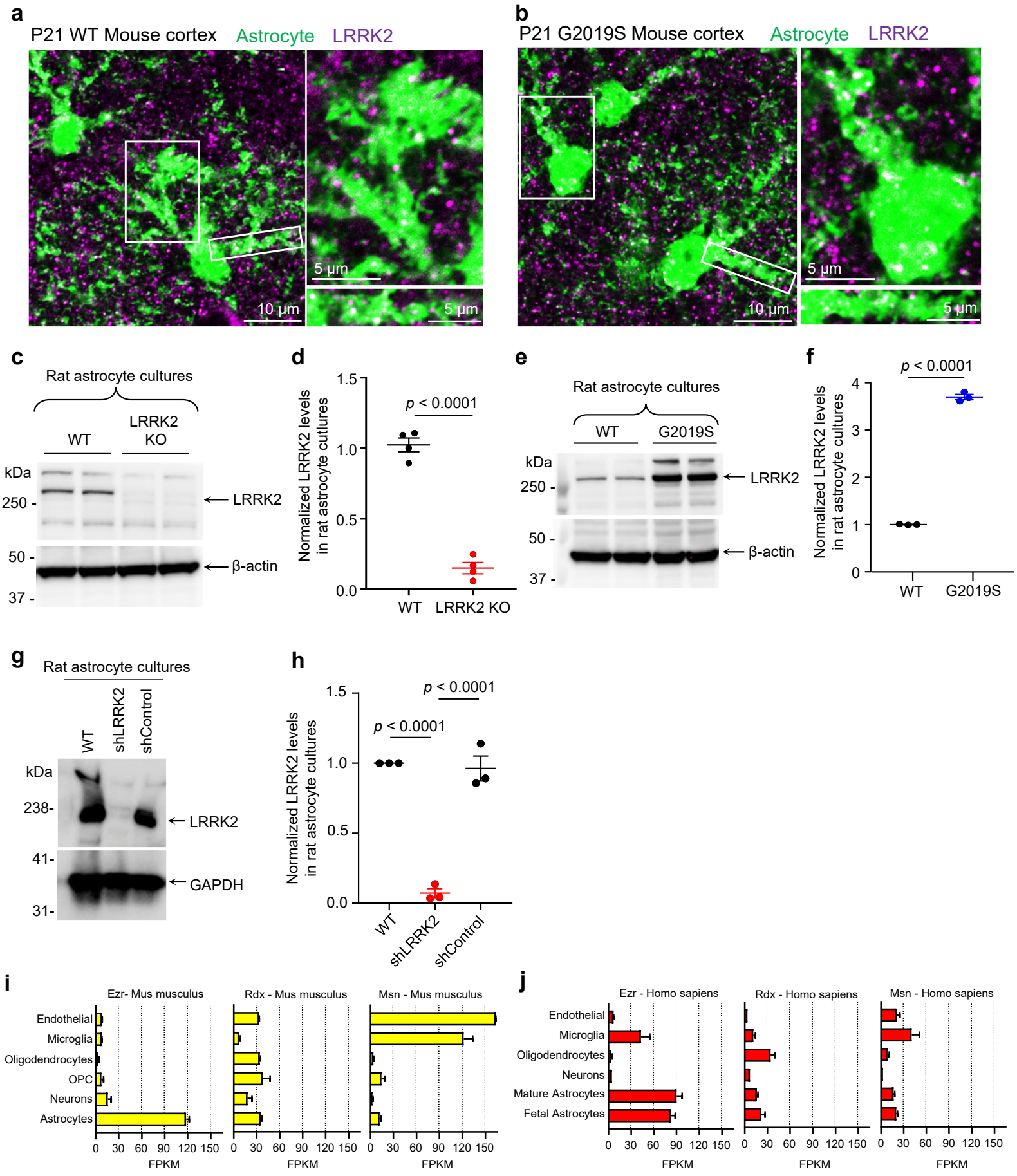

Extended Data Figure 2.

Wang et al.,

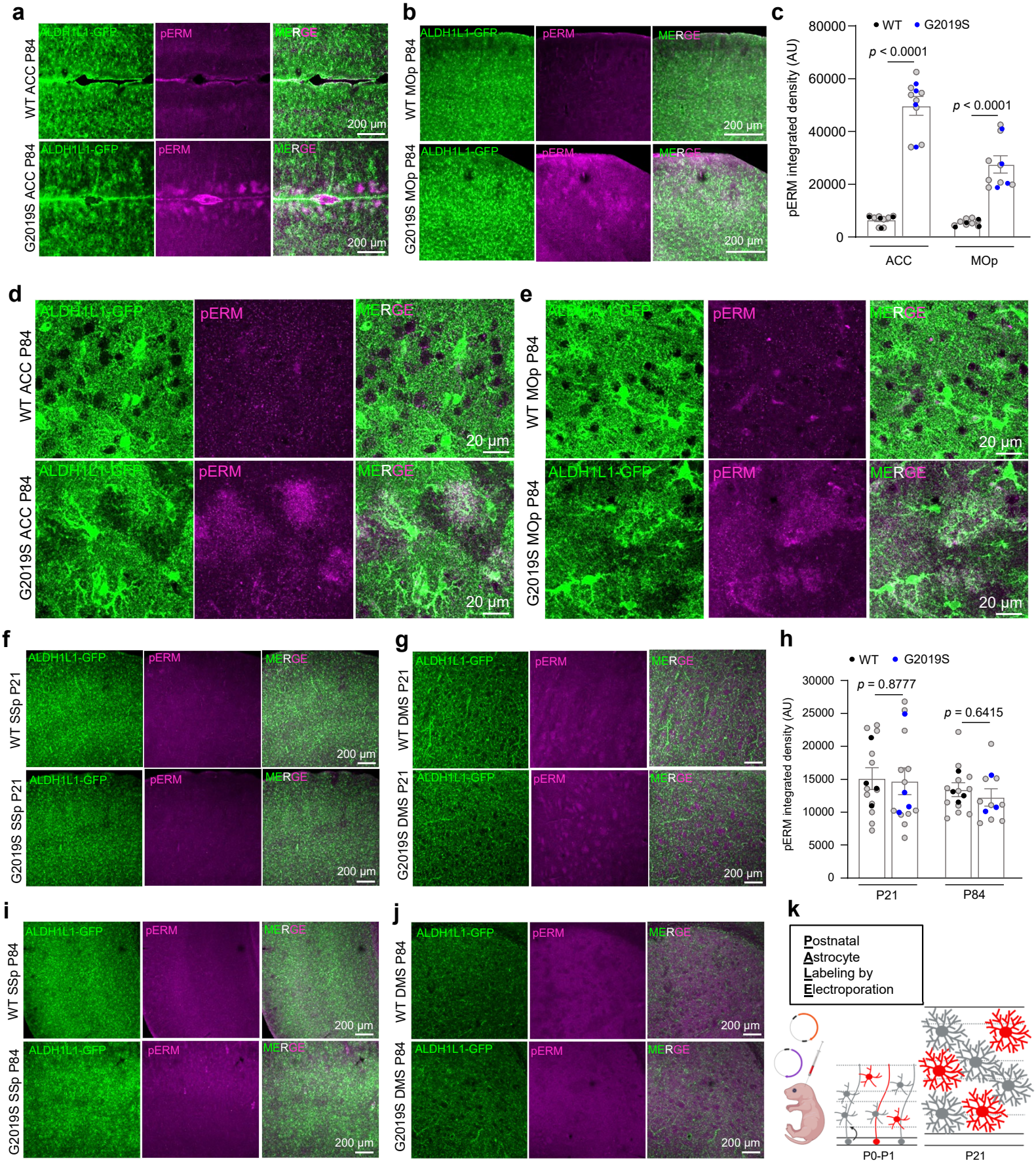

Extended Data Figure 3. Wang et al.,

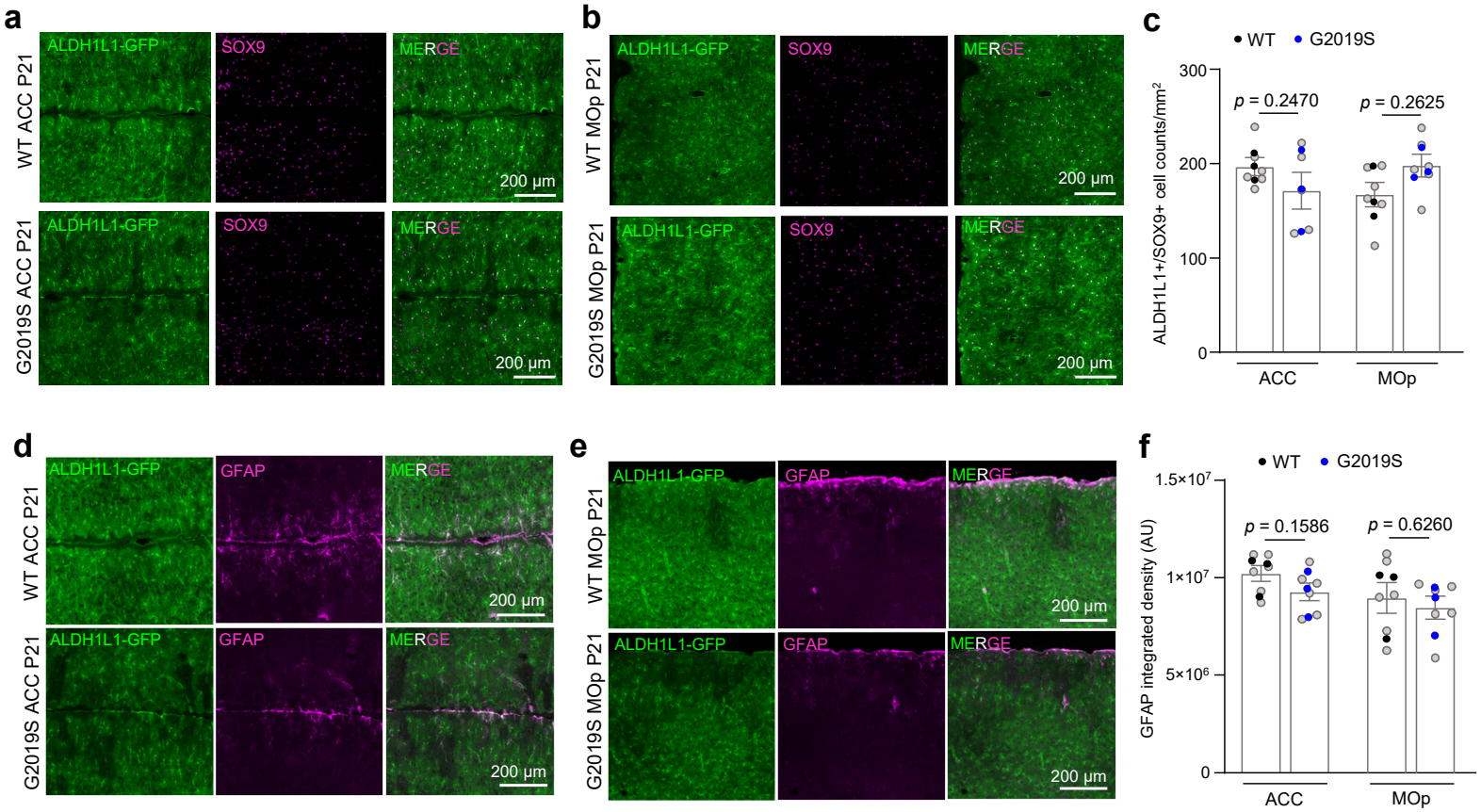

Extended Data Figure 4. Wang et al.,

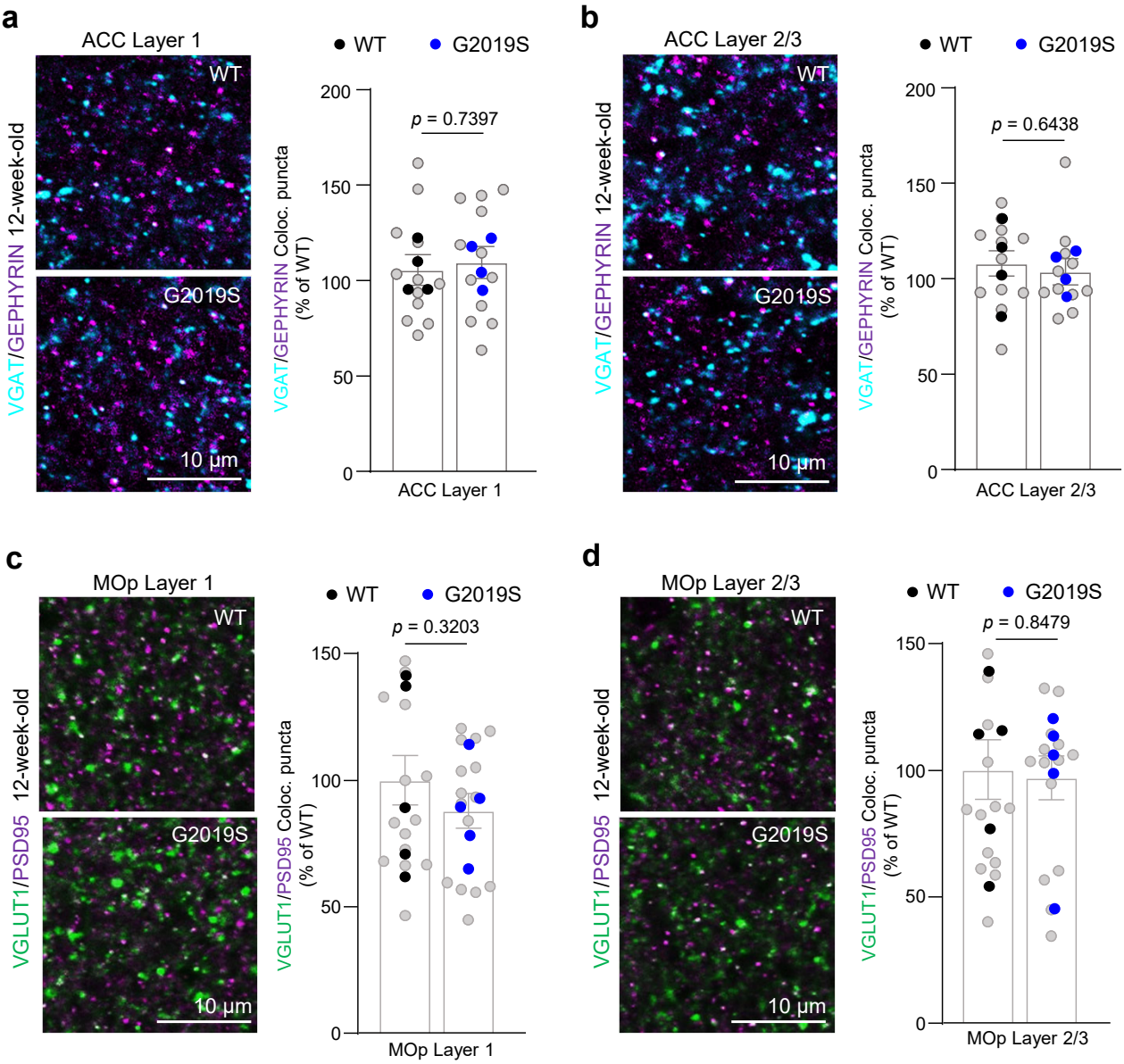
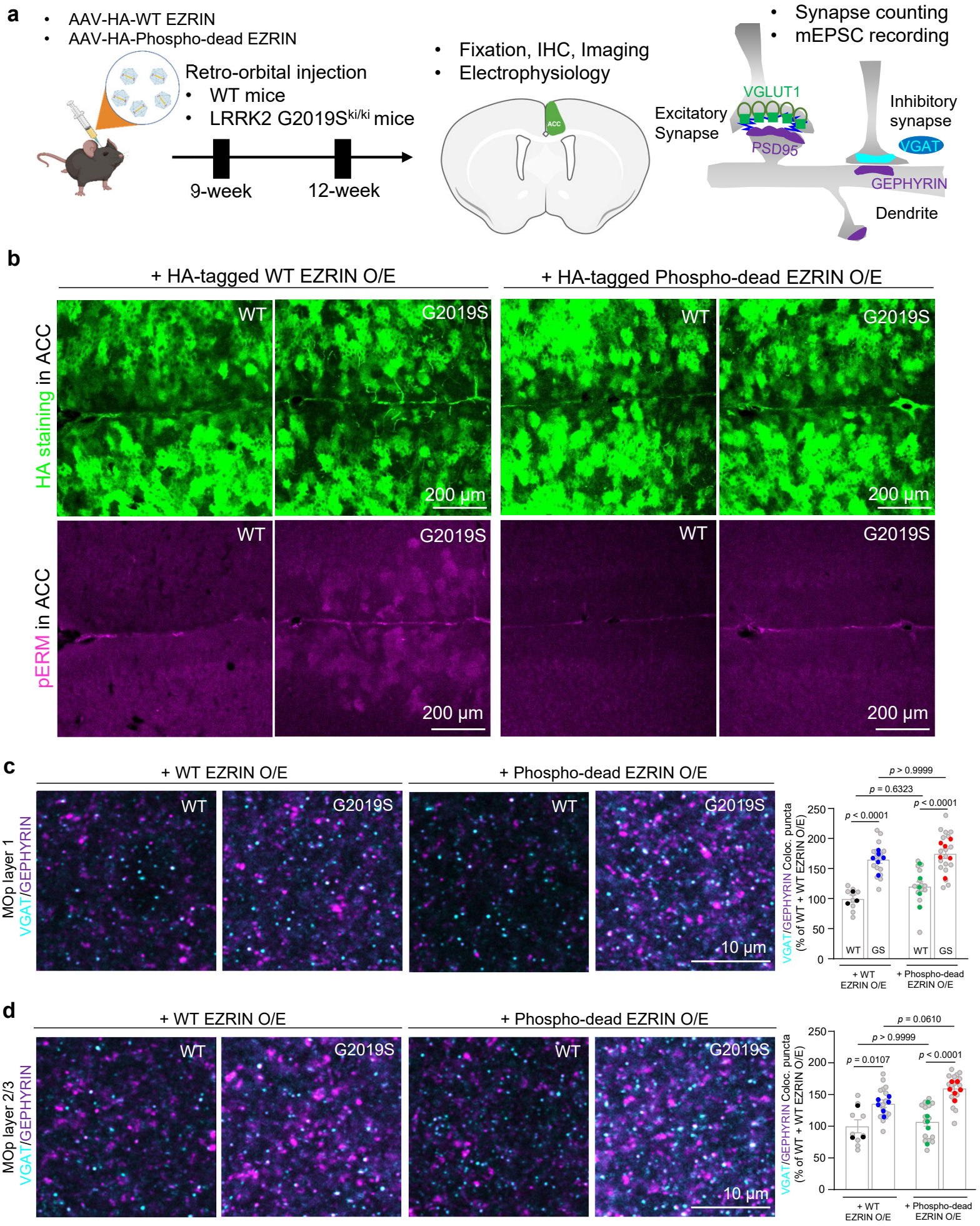
Extended Data Figure 5. Wang et al.,